Multidisciplinary Design Methodology for Micro-Gas-Turbines—Part I: Reduced Order Component Design and Modeling

Lukas Badum
Department of Aerospace Engineering,
Technion, Israel Institute of Technology,
Lady Davis 740,
Technion City, Haifa 320003, Israel
e-mail: lukas@campus.technion.ac.il

Felix Schirrecker
Department of Aerospace Engineering,
Technion, Israel Institute of Technology,
Lady Davis 740,
Technion City, Haifa 320003, Israel
e-mail: sfelix@campus.technion.ac.il

Beni Cukurel[1]
Department of Aerospace Engineering,
Technion, Israel Institute of Technology,
Lady Davis 740,
Technion City, Haifa 320003, Israel
e-mail: beni@cukurel.org

Ultramicrogas turbines (UMGTs) for electric power generation up to 1 kW are a viable replacement technology for lithium batteries in drones due to their high energy density. Previous research has shown that small-scale effects disqualify conceptual design practices applied to larger gas turbines owing to highly coupled, nonlinear component interactions. To fill this gap, we propose an interdisciplinary conceptual design and analysis framework based on reduced order models. To this end, the current work is divided into two parts covering component design and system integration, analysis, and optimization. In Part I, automated conceptual design of all engine subcomponents is elaborated facilitating interdependent reduced order models for compressor, turbine, combustor and high-speed generator while also considering additive manufacturing constraints. In a second step, the reduced order performance models are compared to computational fluid dynamics (CFD) Reynolds-averaged-Navier–Stokes (RANS) simulations of various turbomachinery geometries as well as experimental data of combustor and high-speed generator prototypes, showing good agreement and thus validating the component modules. In conclusion, the first part of this work elaborates an automated and efficient method to conceptual design of all components required for a functional UMGT. Since the strategy is applicable independent of component arrangement and engine layout, the proposed methods offer a universal framework for small gas turbine generators. [DOI: 10.1115/1.4064825]

Introduction

Microturbines are commonly used in applications demanding high power density, fuel flexibility, or combined heat and power. For electric power generation, standard designs on the market today use a recuperated Brayton cycle aiming at a power output between 30 and 200 kW. However, there have been efforts made to scale down microgas turbines even further to reach design power outputs below 1 kW. In this range, they are commonly referred to as UMGT to differentiate them from their larger counterparts. So far, UMGT are not available on the market and development has mostly been conducted in academic research institutions.

Previous Work. Ultramicrogas turbines were first proposed by an MIT research group aiming at a 60 W electric power output unit facilitating silicon wafer photolithographic etching. To achieve maximum efficiency, design turbine inlet temperature (TIT) and pressure ratio were set to 1600 K and 4, respectively [1–6]. The miniature size required by the manufacturing method resulted in design speed above 1,000,000 rpm and high heat transfer rates from turbine to compressor. Ultimately, no successful demonstrator was established owing to air bearing instability, low turbomachinery efficiencies, and diabatic effects. Tohoku University demonstrated the first self-sustained UMGT Brayton cycle of a 100 W scale

engine. The prototype rotor was entirely computerized numerical control machined from titanium alloy. Aiming at a TIT of 1323 K and design pressure ratio of 3, a demonstrator was built with design speed of 870,000 rpm. During testing, bearing instability prevented reaching speeds above 350,000 rpm and thus positive power output was not achieved. More recently, a research group from KIMM developed a recuperated gas turbine with similar cycle parameters as reported by Tohoku University but at design power output of 1 kW at 400,000 rpm. However, the prototype speed was limited by air bearing instability issues, achieving only 280,000 rpm. Besides these three most advanced developmental efforts, a more detailed summary of accomplishments and challenges of the last 30 years in this field can be found in Ref. [7]. While prior contributions provide scientific insight in the design, manufacturing, and performance challenges of UMGT, further research is needed to overcome the remaining technical barriers and realize their full potential as a promising power generation technology for small-scale applications.

In all previous efforts, the conceptual design stage was centered around Brayton cycle models with static turbomachinery efficiencies. After selecting the pressure ratio, TIT, and compressor flow coefficient (and thus rotational speed), UMGT design was split into subcomponents and each element was optimized individually through RANS CFD and finite element method simulations. Consequently, the conceptual design stage was based on best-practice values of large turbomachinery, for example, optimum compressor flow or turbine work coefficients, and system-level design exploration was not considered. This approach is successful for well-understood systems (even at small scale such as

---

turbochargers [8]) but it is not effective for small-scale high-speed UMGTs where interdependencies between components and disciplines are more pronounced and less explored. For example, the selected compressor flow coefficient has a great impact on bearing design, turbine design, rotor size, rotordynamic behavior, temperature distribution, and system mass flowrate, among others [7]. Hence, it is unlikely that selecting compressor flow coefficient according to best aerodynamic component performance also leads to an optimum system solution: bearing technology may not be feasible, turbine efficiency may be low, the rotor may operate close to a critical speed, or generator temperatures may be too high. This example highlights that UMGT conceptual design should not be split into independent subcomponents as system interdependencies would be disregarded.

Motivation. In this light, there is a need to create a framework that organizes turbomachinery, generator, and combustor design modules in a structured and self-supervised manner with as few free parameters as possible to rapidly evaluate a large design space at reasonable computational cost. Covering multidisciplinary interdependencies in the conceptual stage, the system-level performance can then be evaluated with metrics defining constraints and objectives to find optimal conceptual UMGT architectures.

In the scope of this work, we present an integrated, automated design methodology for UMGT components that inherently captures nonlinear and multidisciplinary interdependencies by facilitating experimentally and numerically validated reduced order design and performance models. Hereby, Part I focuses on component-level design. First, aerodynamic design and performance evaluation methods for the centimeter scale compressor and turbine are formulated. Next, the thermal modeling of a porous media microcombustor is discussed. Then, an approach is outlined for design and loss calculation of high-speed electric generators while considering matching conditions with turbomachinery. To substantiate the reduced order component modeling efforts, relatively higher fidelity RANS CFD simulations are conducted on the compressor and turbine, in addition to experimental validation of the combustor and the generator performance predictions. Lastly, the conceptual design framework is finalized by inclusion of diabatic effects, introducing turbomachinery mass flow matching condition, selection of bearings, and electromagnetic assessment of generator topology, offering a fast multidisciplinary approach to estimate performance UMGT components in an engine setting. In Part II, the automized system integration, analysis, and optimization of components are demonstrated to maximize bearing lifetime, thermodynamic efficiency, and specific power for a 300 W engine with two different rotor material scenarios.

Engine Components

There are different approaches to structure the UMGT layout, each with its own advantages. A part of the literature considered configurations integrating the generator or combustor in between turbine and compressor [9,10]. In a previous work [7], we introduced an UMGT engine with overhung rotor configuration, thus thermally decoupling the electric machine and the heat engine, as depicted in Fig. 1.

The heat engine provides useful shaft power by establishing the Brayton cycle. To facilitate compact design and minimize complexity, radial stages are used for compressor and turbine. In this investigation, a porous media reverse flow combustor is facilitated to provide stable, premixed combustion at small scales. To maintain simplicity, recuperation is not considered. On the generator side, the shaft is supported by angular contact ball bearings and the mechanical power is extracted to provide electric output. To this end, a rotating magnetic field is established by a permanent magnet; owing to its low yield strength, a retaining sleeve is pressed on the magnet to maintain permissible stress limits. In the generator stator, phase coils induce voltage while the surrounding stator iron contains and amplifies the magnetic field of the rotor.
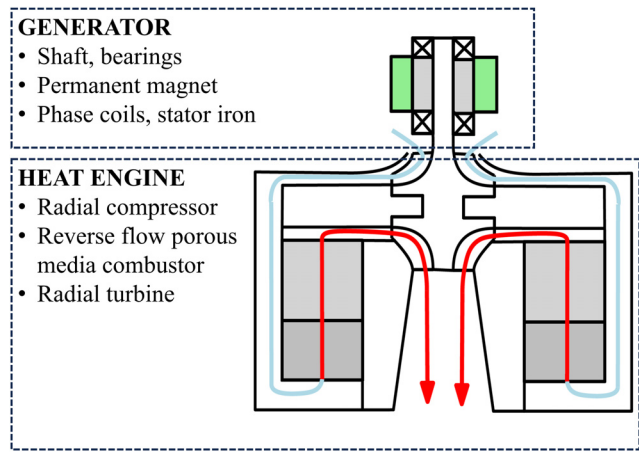

Fig. 1 Microgas turbine engine layout with generator and heat engine components

Reduced Order Design and Performance Assessment

Using reduced order modeling and performance assessment for each component, the compressor, combustor, and turbine form the heat engine, yielding eight free design parameters. After selecting an appropriate bearing for the desired speed, the generator is evaluated based on two additional input parameters while performance is estimated using electromagnetic analysis and subsequent loss modeling. In the conceptual design stage, the individual components are interdependent sharing various parameters such as rotational speed, mass flowrate, aerodynamic conditions, and physical dimensions. This effect is exploited for their design to reduce the number of free variables and generate an effective, automated methodology.

Compressor. Critical to the thermodynamic cycle, the compressor pressure ratio is highly sensitive to rotational speed and mass flowrate, and therefore it is reasonable to initialize the heat engine conceptual design with this component. The compressor shares the system mass flow with all heat engine components

$$\dot{m}_c = \dot{m} \tag{1}$$

Besides this, compressor stage design facilitates four free variables: compressor hub radius ratio ξ_{rh}, work coefficient λ_c, flow coefficient $\phi_{1t,c}$, and rotor total to total pressure ratio $\pi_{tt,r,c}$.

Design Method. The radial compressor is designed to establish the predefined rotor pressure ratio $\pi_{tt,r,c} = P_{2t}/P_{1t}$ at a given flowrate $\dot{m}_c$. Off-design performance is not considered. The meridional flow path and stations are depicted in Fig. 2.
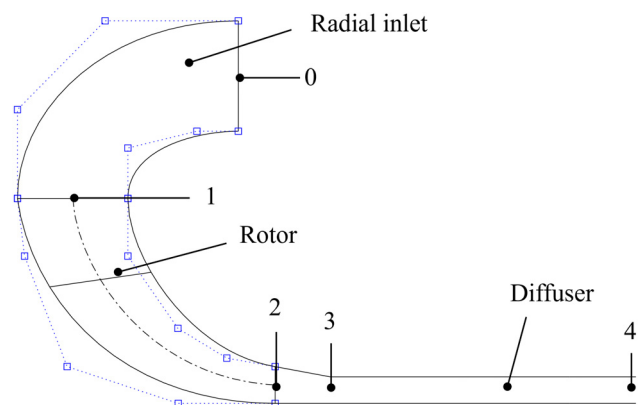

Fig. 2 Compressor rotor and diffuser meridional flow path, numbering conventions

The specific compressor rotor work input w_{12tt} is determined from design pressure ratio $\pi_{tt,r,c}$ and rotor polytropic total-to-total efficiency $\eta_{ptt,r}$

$$w_{12tt} = \frac{1}{\eta_{ptt,r}} \frac{n}{n-1} \cdot RT_1 \left[(\pi_{tt,r,c})^{\frac{n-1}{n}} - 1 \right] \tag{2}$$

$$P_c = w_{12tt}\dot{m}_c \tag{3}$$

For small-scale gas turbines facilitating a single compressor stage, typical rotor pressure ratio ranges between 2 and 5 [7]. To capture heat transfer effects, the diabatic analysis suggested by Casey et al. is implemented [11]. Then, the polytropic exponent n is a function of the normalized heat load factor $\xi_q = q_{12tt}/(w_{12tt}\eta_{ptt,r})$, polytropic efficiency, and specific heat ratio γ

$$n = \left(1 - \left(\left(\xi_q + \frac{1}{\eta_{ptt,r}} \right) \frac{(\gamma-1)}{\gamma} \right) \right)^{-1} \tag{4}$$

Here, the compressor heat load factor is approximated in a separate calculation, as elaborated further on. The rotor enthalpy rise and the tip total temperature are a result of the compressor work input and heat load

$$\Delta h_{12tt} = w_{12tt}(1 + \eta_{ptt,r}\xi_q) \tag{5}$$

$$T_{2t} = T_{1t} + \Delta h_{12tt}/c_p \tag{6}$$

The compressor meanline design provides the flow and work coefficient as free variables

$$\phi_{1t} = \dot{m}/(\rho_{1t}4r_2^3\omega) \tag{7}$$

$$\lambda = \frac{c_{u2}}{u_2} = w_{t12}/u_2^2 \tag{8}$$

Best performance is usually achieved for $\phi_{1t} \sim 0.07$ and $\lambda \sim 0.65$ [12,13]. As mass flowrate and inlet total density are prescribed, the resulting tip radius and rotor speed are now defined.

For an effective inducer, it is desirable to minimize the relative inlet velocity at the blade tip leading edge. This way, the relative velocity levels are moderated, leading to reduced friction losses, secondary losses, and shock losses in the rotor passage [14]. Figure 3 presents the variation of the relative inducer tip velocity $W_{1s} = w_{1s}/u_2$ with tip radius ratio $\xi_{rs} = r_{1s}/r_2$ depending on flow coefficient. For a small inducer tip radius, also the tip circumferential velocity $u_{1s} = \omega r_{1s}$ is low but the meridional inlet velocity c_{m1s} is high owing to a lower frontal inlet area. For the adverse case of a large inducer tip radius, the axial inlet velocity is reduced for the same mass flow while the circumferential velocity is increased for the same rpm. Given a predefined flowrate and rotational speed, it is obvious that an optimum radius ratio exists for which the resulting tip relative velocity $w_{1s} = \sqrt{u_{1s}^2 + c_{m1s}^2}$ is minimized.

Rusch et al. calculated the optimum inducer shroud radius by differentiating the relative inlet Mach number with respect to the radius ratio, but independent of metal blockage and meridional velocity distribution [14]. In small-scale compressors, the blade thickness relative to channel height is enlarged due to manufacturing limitations, and therefore this equation needs to be extended to include a metal blockage factor B_{1m}. Moreover, a radial compressor inlet section is considered in the current engine architecture, resulting in inlet distortions that yield meridional velocity variation from inducer hub to tip. To account for this effect, the meridional velocity ratio $\xi_{cms} = c_{m1s}/c_{m1}$ is incorporated in the calculation of the tip velocity. The resultant modified equation for the optimum tip radius ratio can be represented as

$$\xi_{rs} = \sqrt{\xi_{rh}^2 + 2^{\frac{1}{3}}\left(\frac{4\phi_{1t}}{\pi} \frac{\xi_{cms}}{(1-B_{1m})}\left(1 + \frac{\gamma-1}{2}M_1^2 \right)^{\frac{1}{\gamma-1}} \right)^{\frac{2}{3}}} \tag{9}$$
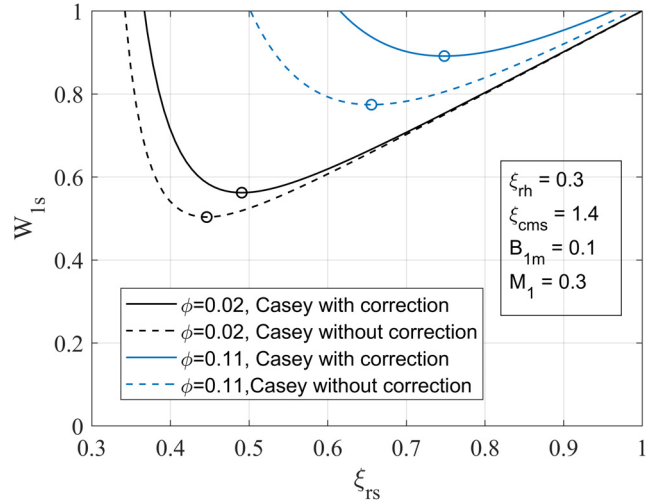

Fig. 3 Variation of relative inlet velocity with shroud radius ratio for different flow coefficients

Figure 3 depicts the relative shroud velocity normalized by the rotor tip speed for two different flow coefficients ϕ_{1t} equal to 0.02 and 0.11. Introducing the discussed corrections has a significant effect on the optimum radius ratio when compared to the original expression. This approach is implemented in the current compressor design methodology while the maximum shroud radius ratio is limited to 0.73 to avoid excessive separation losses, as per recommendations in Ref. [14]. The inlet velocity triangle and blade geometry are then defined based on the metal blockage and meridional velocity distribution, thus requiring only the hub radius ratio $\xi_{rh} = r_{1h}/r_2$ as an additional parameter.

In the rotating frame of reference, the compressor blade passage acts as a diffuser decelerating the flow. To avoid separation, the rotor outlet to inlet shroud tip relative velocity ratio $w_{2,B_2=0}/w_{1s}$, also known as De-Haller number DH, is often prescribed, with typical values ranging between 0.45 and 0.6 [15]. Here, the relative velocity ratio disregards the exit blockage and thus directly describes the rotor outlet geometry. For the small compressors considered, due to the resultant low Reynolds numbers (in the order of 20,000), a conservative value of 0.6 is selected and kept as a constant. To guarantee a realistic geometric tip flow coefficient $\phi_2 = c_{m2,B_2=0}/u_2$, the De-Haller number is adjusted such that ϕ_2 is always greater than or equal to 0.1. This way, the rotor tip velocity triangle is defined and using the aerodynamic blockage B_{2ae} and slip factor σ_2, the tip geometry can be specified

$$w_{2,B_2=0} = w_{1s}DH \tag{10}$$

$$w_{u2} = (\lambda - 1)u_2 \tag{11}$$

$$c_{m2} = (1/(1-B_2))\sqrt{\left(w_{1s}^2/u_2^2 \right)DH^2 - (1-\lambda)^2}\, u_2 \tag{12}$$

$$\tan\beta_{2b} = (c_{u2}/\sigma_2 - 1)u_2/c_{m2} \tag{13}$$

$$A_{2,\text{passage}} = \dot{m}_c/((1-B_{2ae})c_{m2}\rho_2) \tag{14}$$

Then, the compressor axial length and number of blades are selected according to best-practice guidelines described in Ref. [15].

Subsequently, the meridional flow path is generated connecting the calculated support points with Bezier splines. The rotor blade angles with respect to the meridional direction (beta angle) at hub and shroud are calculated using Aungier's definition [13]. Rotor tip clearance is determined from the outlet blade height with a minimum value of 100 μm due to assembly tolerance limitations

$$e_{cl} = 0.05b_2, \quad e_{cl} \geq 0.1 \, \text{mm} \tag{15}$$

The blade thickness is normalized with respect to the tip width with a minimum value due to manufacturing limitations

$$t_b = 0.08b_2, \quad t_b \geq 0.3 \, \text{mm} \tag{16}$$

Performance Model. Compressor rotor performance prediction requires a consistent model for efficiency, tip blockage, and slip factor as all three affect the required work input and thus the tip design. Aungier published a coherent calculation framework of these parameters based on experimental data of industrial compressors [13,16], widely used in literature owing to high prediction accuracy for pressure ratios up to 3.5 [16]. The losses are separated into internal and external sources, comprised of inducer diffusion and choking loss, passage friction loss, blade and hub-to-shroud loading loss, discharge distortion loss, wake mixing loss and tip clearance loss, and comprised of leakage, recirculation, and disk friction losses, respectively.

For a specific desired pressure ratio, the internal rotor losses increase the required rotor tip speed as they reduce the aerodynamic momentum at the rotor exit. For the small-scale compressors investigated, tip clearance, passage friction, and blade loading loss are found to be dominant. In contrast, external losses have no effect on the aerodynamic momentum and thus total pressure ratio; nevertheless, they increase the required shaft power to achieve the design tip speed, thus reducing available net power to the generator. A detailed description of each loss model can be found in Ref. [16], and the framework is extended by the normal shock equation at the compressor inducer to account for a total pressure drop if supersonic conditions are reached in the relative frame. Hereby, the total temperature over the shock is constant while the relative total pressure after the shock $P'_{1t,as}$ is calculated from the relative total pressure before the shock, $P'_{1t,bs}$

$$\frac{P'_{1t,as}}{P'_{1t,bs}} = \left[\frac{(\gamma+1)M'^2_1}{(\gamma-1)M'^2_1 + 2} \right]^{\frac{\gamma}{\gamma-1}} \left[\frac{\gamma+1}{2\gamma M'^2_1 - (\gamma-1)} \right]^{\frac{1}{\gamma-1}} \tag{17}$$

Furthermore, it was discovered during CFD analysis that Aungier's model overestimates recirculation losses for small-scale compressors. The original recirculation loss model is modified by a linear factor

$$\Delta h_{re} = 0.3 \Delta h_{re,\text{Aungier}} \tag{18}$$

In addition, a vaneless diffuser is designed based on best-practice guidelines from Refs. [17,18]. The ratios of the inner and outer radius to the compressor tip radius are fixed at 1.15 and 1.8, respectively. If necessary, the diffuser channel width is reduced by pinch such that the absolute tip flow angle does not exceed 65 deg, see station 3 in Fig. 2. For the vaneless diffuser, a finite difference calculation according to Stanitz [19] is employed facilitating a local friction factor depending on the flow path length, as suggested by Japikse [20]

$$c_{f,vd} = k \text{Re}_x^{0.2} \tag{19}$$

with $\text{Re}_x = cx/\nu$, where c and x denote the absolute flow velocity and the flow path length of a logarithmic spiral through the diffuser, respectively. Japikse presented local friction factor measurements of different diffusers indicating a variation of k between 0.03 and 0.2; in this case, $k = 0.07$ is implemented.

Finally, the total-to-total rotor and stage aerodynamic efficiencies can be written as follows:

$$\eta_{\text{ptt},r} = \frac{n}{n-1} \cdot \frac{RT_1 \left[(\pi_{12tt})^{\frac{n-1}{n}} - 1 \right]}{\frac{n}{n-1}RT_1 \left[(\pi_{12tt})^{\frac{n-1}{n}} - 1 \right] + \sum \Delta h_{l,\text{rotor}}} \tag{20}$$

$$\eta_{\text{ptt}} = \frac{n}{n-1} \cdot \frac{RT_1 \left[(\pi_{14tt})^{\frac{n-1}{n}} - 1 \right]}{\frac{n}{n-1}RT_1 \left[(\pi_{14tt})^{\frac{n-1}{n}} - 1 \right] + \sum \Delta h_{l,\text{rotor}} + \sum \Delta h_{l,\text{parasitic}}} \tag{21}$$

The specific shaft work required to drive the compressor at the design point is given by

$$w_c = w_{12tt} + \sum \Delta h_{\text{loss,parasitic}} \tag{22}$$

Then, the state conditions and velocities can be calculated iteratively for all compressor stations. Efficiency, blockage, and slip factor are updated according to the selected models until convergence is reached.

Combustor. Large gas turbines use diffusion burners with a primary mixing zone and a secondary dilution zone where average flow velocities are between 50 and 100 m/s. However, this is not practical for small engines because the required time for fuel evaporation, reaction, and dilution leads to disproportionately large combustors. Therefore, a porous inert media combustor is suggested as alternative technology, utilizing foam like ceramic or metal materials to sustain premixed combustion. The large surface area of the foam preheats the reactants and, together with the self-irradiation benefits of each porous cavity, allows for stable combustion at low equivalence ratios while the inert material acts as a heat storage to prevent flame-out. Porous media combustors have been studied for use with both gaseous and liquid fuels [21–25]. Accordingly, a simplified method for designing and modeling a porous media combustor for an UMGT is presented. The combustor shares the system mass flowrate while the inlet thermodynamic conditions are prescribed by the compressor exit

$$P_{\text{cc,in}} = P_{4t,c} \tag{23}$$

$$T_{\text{cc,in}} = T_{4t,c} \tag{24}$$

Design Method. The combustor is modeled using a simple first-law analysis considering compressor outlet conditions, design turbine inlet temperature, chemical combustion efficiency, and heat losses

$$\Delta h_{cc} = \int_{T_{4t,c}}^{\text{TIT}} c_p(T)dT / \eta_{\text{chem}} + q_{\text{loss}} \tag{25}$$

Heat capacity is modeled as function of temperature and gas composition using tabular thermodynamic functions from NASA Lewis Coefficients [26]. Hence, the resulting fuel mass flow and required combustor heat input are

$$\dot{m}_f = \dot{m} \frac{\Delta h_{cc}}{\text{LHV}} \tag{26}$$

$$\dot{Q}_{cc} = \dot{m} \Delta h_{cc} \tag{27}$$

The combustor is designed to satisfy a sufficient Damköhler number, ratio of residence time to chemical reaction time, as suggested in Ref. [27]

$$\text{Da} = \tau_{\text{res}} / \tau_{\text{chem}} = 5 \tag{28}$$

Chemical reaction time scale is determined from thermal diffusion and laminar flame speed. The latter is a function of equivalence ratio, pressure, and temperature and is estimated for evaporated kerosene based on empirical polynomials following Ref. [28]. The resulting outer combustor radius is calculated using the turbine outlet shroud radius $r_{4s,t}$, required system mass flowrate $\dot{m}$, and average flow velocity $\bar{c}_{cc}$

$$r_{cc,o} = \sqrt{\frac{\dot{m}}{\bar{\rho}_{cc}\bar{c}_{cc}\pi} + r_{4s,t}^2} \tag{29}$$

$$l_{cc} = \bar{c}_{cc}\tau_{\text{chem}}\text{Da} \tag{30}$$

The average flow velocity is a fixed parameter obtained from experimental tests. A value of 3 m/s showed to be a good compromise between stability and lean limit. The design calculation is iterated until sufficient convergence of fuel mass flow is achieved.

Performance Model. Combustor efficiency is penalized by conductive, convective, and radiative heat losses. Owing to the high foam temperature and radiative heat transfer scaling with T^4, it can be shown that radiation heat loss is the dominant mechanism for porous media combustors with exhaust temperatures above 1200 K [29]. To this end, the porous media foam is considered as a radiating surface with a uniform temperature and a view factor to both axial ends of the combustion chamber as depicted in Fig. 4. The effective foam temperature is estimated to be the averaged of equivalence ratio dependent adiabatic flame temperature and the turbine inlet temperature after heat losses

$$T_{\text{foam}} = (\text{AFT}(\phi) + \text{TIT})/2 \tag{31}$$

The ceramic foam radiates toward two axial casing end surfaces: the turbine side casing and the compressor side casing with radiative heat fluxes $\dot{Q}_{\text{rad},t}$ and $\dot{Q}_{\text{rad},c}$, respectively. Then, the casing temperature is estimated as an average of compressor exit and turbine inlet temperatures

$$T_{\text{casing}} = (T_{4t,c} + \text{TIT})/2 \tag{32}$$

Since the flame front is assumed to settle in between the two porous media foams and the foams have different porosity and associated optical permeability, the view factors differ; in this case, values of $F_t = 0.5$ and $F_c = 0.8$ are selected. Using the foam emissivity of $\epsilon_{\text{foam}} = 0.8$ and $\epsilon_{\text{casing}} = 0.5$ according to material data, the radiative heat flux contributions can be determined

$$\dot{Q}_{\text{rad},c} = \frac{\sigma\left(T_{\text{foam}}^4 - T_{\text{casing}}^4\right)}{\frac{1-\epsilon_{\text{foam}}}{A_{\text{rad}}\epsilon_{\text{foam}}} + \frac{1}{A_{\text{rad}}F_c} + \frac{1-\epsilon_{\text{casing}}}{A_{\text{rad}}\epsilon_{\text{casing}}}} \tag{33}$$

$$\dot{Q}_{\text{rad},t} = \frac{\sigma\left(T_{\text{foam}}^4 - T_{\text{casing}}^4\right)}{\frac{1-\epsilon_{\text{foam}}}{A_{\text{rad}}*\epsilon_{\text{foam}}} + \frac{1}{A_{\text{rad}}F_t} + \frac{1-\epsilon_{\text{casing}}}{A_{\text{rad}}*\epsilon_{\text{casing}}}} \tag{34}$$

In addition to radiation, also convective heat losses are considered assuming a uniform foam temperature equal to TIT and fluid temperature e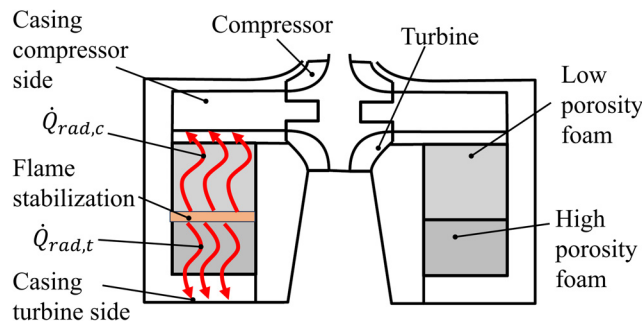qual to compressor exit. The forced convection heat transfer coefficient at the outer surface of the foam is estimated with a value of 50 W/(m²K)

$$\dot{Q}_{\text{conv}} = 50A_{\text{conv}}(\text{TIT} - \text{CET}), \quad A_{\text{conv}} = 2\pi r_{\text{foam}}l_{\text{foam}} \tag{35}$$

Since the foam outer radius temperature can be minimized using insulation around the porous media, this correlation presents a conservative approach. However, heat is inevitably transferred to the adjacent casing components by conduction and subsequently absorbed by the fluid flow. Therefore, since the precise geometry of the engine is not known in the preliminary design stage, this calculation is a reasonable approach to estimate convective heat losses. By adding convective and radiative heat losses, the specific heat loss of the combustor is found and can be used to iteratively find the required fuel flowrate. Additionally, the pressure drop of the combustor is modeled using a semi-empirical calculation method based on the bulk flow velocity and density [30]

$$\Delta P/l_{cc} = \mu\bar{c}_{cc}/k_{1,cc} + \bar{\rho}_{cc}\bar{c}_{cc}^2/k_{2,cc} \tag{36}$$

For the permeability constants, empirical values for oxide-bond silicon carbide foams are used, $k_{1,cc} = 56 \cdot 10^{-9}$ m² and $k_{2,cc} = 123 \cdot 10^{-5}$ m according to Ref. [30]. This calculation is found to agree well with preliminary experimental differential pressure measurements with and without porous foam. Due to the comparatively large combustor size and subsequent low flow velocity, the resulting pressure drop is well below 1% of the total inlet pressure.

Turbine. The turbine provides useful shaft work by expanding the hot gases leaving the combustor. It furthermore shares the system rotational speed and flowrate with the compressor, while inlet aerodynamic conditions are prescribed by the combustor outlet

$$P_{1t,t} = P_{cc,\text{out}} \tag{37}$$

$$T_{1t,t} = T_{cc,\text{out}} = \text{TIT} \tag{38}$$

Besides this, only the turbine outlet flow coefficient ϕ_4 and work coefficient λ are facilitated as free design variables.

Design Method. Located on the same shaft as the radial compressor, the turbine is designed to expand the high pressure and temperature flow leaving the combustor to ambient pressure at the exhaust. Figure 5 depicts the meridional cross section and the notation convention.

The specific turbine rotor work output w_{34tt} is calculated from inlet conditions, rotor efficiency, and total-to-total expansion ratio

$$w_{34tt} = \eta_{\text{ptt},r}\frac{n}{n-1} \cdot RT_3\left[\left(\epsilon_{34tt}\right)^{\frac{n-1}{n}} - 1\right] \tag{39}$$

Fig. 4 Porous media combustor components, flame position, and resulting radiative heat losses toward axial end surfaces
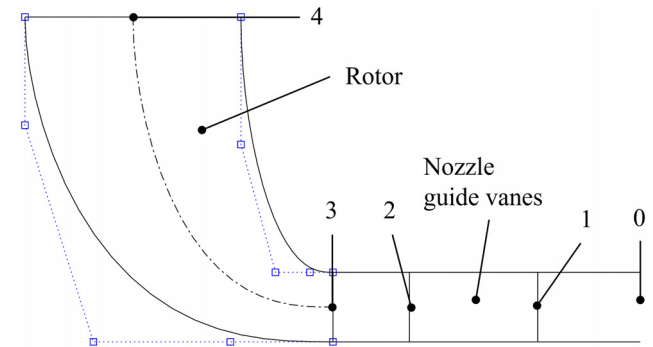

Fig. 5 Turbine stator and rotor meridional flow path including numbering conventions

$$P_t = w_{34tt}\dot{m}_t \qquad (40)$$

While the static pressure at the turbine exhaust is given by ambient conditions, the total-to-total expansion ratio is not known a priori as it depends on outlet Mach number, stage efficiency, and mass flowrate, and therefore must be determined iteratively from the combustor outlet conditions. Applying the diabatic analysis [31], it can be shown that the turbine work is reduced due to heat extraction and the polytropic exponent n can then be written as

$$n = \left(1 - \left((\xi_q + \eta_{\mathrm{ptt},r})\frac{(\gamma - 1)}{\gamma}\right)\right)^{-1} \qquad (41)$$

The change in rotor enthalpy and total temperature can be calculated from the turbine work input and heat load

$$\Delta h_{34tt} = w_{34tt}\left(1 + \xi_q/\eta_{\mathrm{ptt},r}\right) \qquad (42)$$

$$T_{4t} = T_{3t} + \Delta h_{34tt}/c_p \qquad (43)$$

Since the turbomachinery components rotate on the same shaft, the compressor design dictates the turbine rotational speed, thus reducing the number of free design variables. Using the diabatic work input, the turbine design is based on the outlet flow and work coefficient, which are considered to dominate the performance, while best performance is obtained typically for $\phi_4 \sim 0.25$ and $\lambda \sim 0.85$ [32]

$$\phi_4 = c_{m4}/u_3 \qquad (44)$$

$$\lambda = w_{34tt}/u_3^2 = (u_4c_{u4} - u_3c_{u3})/u_3^2 \qquad (45)$$

From the rotational velocity of the compressor, the turbine tip radius and speed are calculated

$$r_3 = \frac{\left(-\frac{w_{34tt}}{\lambda}\right)^{0.5}}{\omega_c} \qquad (46)$$

$$u_3 = r_3\omega_c \qquad (47)$$

To minimize blade root stresses, turbine rotors can be equipped with purely radial leading edges corresponding to an inlet blade angle of $0°$ [33], an approach that is also adapted in this work. The circumferential velocity component at rotor inlet is given from the work coefficient, radius ratio, and outlet swirl velocity

$$c_{u3} = \lambda u_3 + r_4/r_3 c_{u4} \qquad (48)$$

To further define inlet velocity triangle and blade height, the meridional velocity ratio from rotor inlet to outlet is used

$$\xi_{cm} = c_{m4}/c_{m3} \qquad (49)$$

$$c_{m3} = \phi_4 u_3/\xi_{cm} \qquad (50)$$

$$b_3 = \dot{m}/(2\pi r_3 \rho_3 c_{m3}) \qquad (51)$$

As a design guideline for optimum flow and work coefficients, $\xi_{cm} = 1$ is suggested [34,35]. However, for low outlet flow and high work coefficients, this value results in disproportionate nozzle guide vane (NGV) channel height; the exit meridional velocity is reduced and consequently the inlet channel height is increased to maintain proportional reduction of inlet meridional velocity. It is observed that critical NGV (Nozzle Guide Vane) channel heights are reached for flow coefficients below 0.2, and a similar effect is observed for work coefficients above 1, wherein these designs result in a disproportionate NGV channel height to compensate for the reduced inlet radius while maintaining a constant meridional velocity from inlet to outlet. To adapt the design strategy, the meridional velocity ratio ξ_{cm} is linearly interpolated from 1.5 to 1 for flow coefficients ϕ_4 between 0.1 and 0.2 and work coefficients λ from 1 to 1.2.

At the turbine exit, the outlet hub radius ratio is prescribed. In literature, values between 0.185 and 0.3 can be found [36–38]. Since

the blade thickness of small rotors is disproportionately large, a low hub radius ratio limits the number of blades as the circumferential space at the outlet hub is reduced. In the scope of this work, preliminary CFD and structural analysis on a prototype turbine showed that good aerodynamic performance and structural integrity is achieved with a value of 0.28, see Ref. [39]

$$\xi_{r4h} = r_{4h}/r_3 = 0.28 \qquad (52)$$

Then, together with the outlet flow coefficient, the exit shroud and mean radius and circumferential velocity are determined

$$r_{4s} = \sqrt{\xi_{r4h}^2 r_3^2 + \frac{\dot{m}}{\pi\rho_4\phi_4 u_3}} \qquad (53)$$

$$r_4 = (r_{4s} + \xi_{r4h}r_3)/2 \qquad (54)$$

$$u_4 = r_4\omega_c \qquad (55)$$

The turbine exit blade angle is designed to yield zero swirl velocity for minimum kinetic losses, as is common practice in literature [33,35]. However, to facilitate support-free additive manufacturing, the average exit blade is limited to 55 deg to avoid overhung and resulting surface quality degradation

$$\beta_4 = \mathrm{atan}(-u_4u_3/\phi_4), \quad \beta_4 \geq -55 \text{ deg} \qquad (56)$$

Thus, kinetic exit losses and efficiency reduction due to residual swirl are tolerated. The residual exit swirl velocity can be estimated assuming perfect flow guidance

$$c_{u4} = \tan(\beta_4)\phi_4 u_3 + u_4 \qquad (57)$$

Other geometric rotor parameters like blade number and axial length are selected according to best practice guidelines, as suggested by Ventura [35]. Once the rotor geometry is defined, the nozzle guide vane geometry is generated such that the spacing to throat ratio provides the required inlet flow angle [38]

$$\alpha_3 = \alpha_2 = \mathrm{atan}(c_{u3}/c_{m3}) \qquad (58)$$

$$o_2/s_2 = \sin(\alpha_2) \qquad (59)$$

The rotor tip clearance and blade thickness are referenced to the outlet blade height (similar to compressor design Eqs. (15) and (16)) with a minimum radial tip clearance and blade thickness of 0.2 mm and 0.3 mm, respectively. The design calculations are iterated, and thermodynamic quantities are updated until convergence of flowrate, Mach numbers and total temperatures.

Performance Model. According to a comparative study [40], the existing turbine loss models currently available in open literature are applicable only to a narrow design space, stemming from stages with optimum design parameters. In the scope of this work, it is desirable to explore a wider design space to find optimal solutions for the system that potentially compromise on turbine efficiency; therefore, a set of loss models are combined to yield best agreement with numerical results for the small-scale radial turbine. Hereby, turbine rotor efficiency is determined by incidence, passage, tip clearance, friction, and trailing edge losses.

Optimum rotor efficiency is typically achieved for a negative leading edge incidence of $\beta_{3,\mathrm{id}} \sim -30°$, due to the formation of Coriolis force induced vortices in the turbine blade passage [33,41]. While radial turbines are commonly designed to operate under the optimum incidence at the design point, this approach constraints the work coefficient, thus preventing design space exploration. In this work, turbine rotors are allowed to endure significant incidence and the associated entropy production, depending on the design parameters. Incidence losses are commonly considered to stem

from a deviation of the relative inlet flow angle from its optimal value, and they can be estimated based on the number of radial rotor blades [42], as

$$c_{u3,\text{id}} = u_3 \left(1 - \frac{2 \sin\left(\frac{\pi}{Z_r}\right)}{\pi \left(1 + \sin\left(\frac{\pi}{Z_r}\right)\right)} \right) \tag{60}$$

$$\tan\left(\beta_{3,\text{id}}\right) = \left(c_{u3,\text{id}} - u_3\right)/c_{m3} \tag{61}$$

$$i_3 = \beta_3 - \beta_{3,\text{id}} \tag{62}$$

The kinetic energy of the circumferential velocity deviating from the ideal incidence angle is assumed to be lost [43]

$$\Delta h_i = 0.5 w_3^2 \sin^2(i_3) \tag{63}$$

In addition to incidence dependent entropy production mechanism, passage losses associated with secondary flows are also considered, and it is well established that they scale with relative flow velocity and dominate the total rotor entropy production over a wide design space [35,38,40,43]. In the current performance model, they are calculated according to Ref. [34], with a correction term on the relative velocity accounting for the incidence losses [44]

$$w_{3,i} = \sqrt{2\left(\Delta h_i + \frac{w_3^2}{2}\right)} \tag{64}$$

$$\Delta h_p = k_p \frac{W_{3,i}^2 + W_{3s}^2}{2} \tag{65}$$

The empirical coefficient k_p varies between 0.2 and 0.44 for different turbine stages [34], and in the scope of this work, $k_p = 0.4$ is used.

Moreover, tip clearance losses are induced by leakage flow from pressure to suction side over the blade tip. It has been experimentally observed that the radial clearance is more significant for rotor efficiency than axial clearance [40] and the best fit with experimental data is shown with the following correlation [45]:

$$\Delta h_{\text{cl}} = k_{cl} \frac{e_{\text{cl,r}}}{b_3} c_{\text{u3}} \left[\frac{4\pi}{b_3 Z_r} \frac{r_{4s}^2 - r_{4h}^2}{(r_3 - r_{4s})} c_{u3} c_{4m} \frac{1}{1 + \frac{\rho_3}{\rho_4}} \right]^{0.5} \tag{66}$$

In the scope of this work, the value of k_{cl} was increased from 0.6 to 0.8 to account for the disportionally large tip clearance, as compared to the experimental data originally used by Jansen. The friction losses are calculated using passage hydraulic length over diameter ratio and a corrected friction factor for turbomachinery, as suggested by Ventura [35]

$$\Delta h_f = c_{f,p} \frac{L_h}{D_h} \frac{(w_3 + w_4)^2}{4} \tag{67}$$

Trailing edge losses are modeled using a Borda–Carnot equation for a sudden expansion loss [13]

$$\Delta h_{\text{te}} = 0.5 \left(\frac{Z_r t_b b_4}{\pi \left(r_{4s}^2 - r_{4h}^2\right) \cos(\beta_{4b})} \right)^2 c_{m4}^2 \tag{68}$$

The nozzle static enthalpy losses can be calculated based on an empirical correlation according to Rodgers assuming smooth blades [46]

$$\Delta h_n = c_{f,n} \frac{c_2^2}{2} \tag{69}$$

$$c_{f,n} = \frac{0.05}{Re_n^{0.2}} \left(3 \tan(\alpha_3) \frac{c_n}{s_n} + \cos(\alpha_3) \frac{s_n}{b_3} \right) \tag{70}$$

Here, the nozzle Reynolds number is based on the trailing edge velocity and vane height. Lastly, the disk friction losses can be estimated by the same empirical equations as described for the compressor [13]. Then, the total-to-total rotor and stage aerodynamic efficiencies can be written as follows:

$$\eta_{\text{ptt},r} = \frac{\frac{n}{n-1} \cdot RT_3 \left[(\epsilon_{34tt})^{\frac{n-1}{n}} - 1 \right] + \sum \Delta h_{\text{loss,rotor}}}{\frac{n}{n-1} \cdot RT_3 \left[(\epsilon_{34tt})^{\frac{n-1}{n}} - 1 \right]} \tag{71}$$

$$\eta_{\text{ptt}} = \frac{\frac{n}{n-1} \cdot RT_3 \left[(\epsilon_{34tt})^{\frac{n-1}{n}} - 1 \right] + \sum \Delta h_{\text{loss,rotor}} + \sum \Delta h_{\text{loss,parasitic}}}{\frac{n}{n-1} \cdot RT_3 \left[(\epsilon_{14tt})^{\frac{n-1}{n}} - 1 \right]} \tag{72}$$

The net-specific shaft work provided by the turbine at the design point is given by

$$w_t = w_{34tt} + \sum \Delta h_{\text{loss,parasitic}} \tag{73}$$

Estimation of Diabatic Effects on Turbomachinery Components. To consider the diabatic effects on turbomachinery components during the iterative heat engine design cycle, compressor and turbine heat loads are estimated using a heat transfer network model with two elements and three nodes, Fig. 6. The shaft heat input is estimated from an assumed electromechanical generator efficiency

$$\dot{Q}_{\text{shaft}} = P_{\text{shaft}}(1 - \eta_{el}\eta_m) \tag{74}$$

Subsequently, the element conductance is determined based on preliminary rotor geometry assumptions as follows:

$$r_{o,\text{im}} = r_{c2}/2 \tag{75}$$

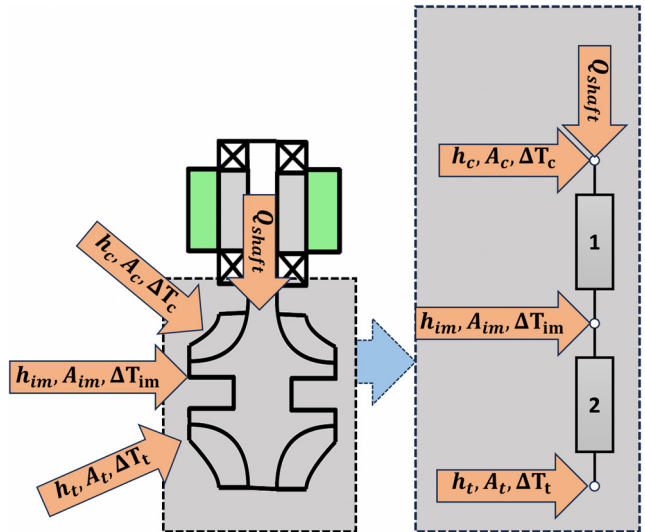$$r_{i,\text{im}} = r_{c2} - t_{\text{im}} \tag{76}$$

$$l_{\text{im}} = r_{c2}/3 \tag{77}$$

Fig. 6 Turborotor preliminary heat load analysis: three-dimensional model, boundary conditions, and resulting thermal network

$$c_{\mathrm{im}} = k\pi\left(r^2_{o,\mathrm{im}} - r^2_{i,\mathrm{im}}\right)/l_{\mathrm{im}} \tag{78}$$

$$A_{im} = 2\pi r_{o,\mathrm{im}}l_{im} \tag{79}$$

The temperature of the casing section adjacent to the rotor is estimated as the mean between compressor exit and turbine inlet total temperatures

$$T_{\mathrm{casing}} = (T_{2t,c} + T_{3t,t})/2 \tag{80}$$

The average flow temperature of turbine and compressor is calculated using results of the turbomachinery design

$$T'_{c,\mathrm{flow}} = \left(T'_{1t,c} + T'_{2t,c}\right)/2 \tag{81}$$

$$T'_{t,\mathrm{flow}} = \left(T'_{3t,t} + T'_{4t,t}\right)/2 \tag{82}$$

To estimate heat transfer coefficients, turbine and compressor blade passages are modeled as flat plates with fins [47], using the relative mean passage velocity and fluid conditions between the inlet and the outlet. The convective heat transfer coefficient inside the rotating gap between the intermediate section and its outer casing is considered using a Nusselt correlation according to Ref. [48]. This results in the following formulation for the solid temperature distribution:

$$
\begin{pmatrix}
c_{\mathrm{im}} + h_c A_c & -c_{\mathrm{im}} & 0 \\
-c_{\mathrm{im}} & 2c_{\mathrm{im}} & -c_{\mathrm{im}} \\
0 & -c_{\mathrm{im}} & c_{\mathrm{im}} + h_t A_t
\end{pmatrix}
\cdot
\begin{pmatrix}
T_c \\
T_{\mathrm{im}} \\
T_t
\end{pmatrix}
$$
$$
=
\begin{pmatrix}
\dot{Q}_{\mathrm{shaft}} + h_c A_c T'_{c,\mathrm{flow}} + \dot{Q}_{c,\mathrm{blade}} \\
h_{\mathrm{im}} A_{\mathrm{im}} T_{\mathrm{casing}} \\
h_t A_t T'_{t,\mathrm{flow}} + \dot{Q}_{t,\mathrm{blade}}
\end{pmatrix} \tag{83}
$$

Subsequently, turbine and compressor heat load factors can be determined

$$\xi_{q,c} = h_c A_c (T_{c,\mathrm{flow}} - T_c)/(w_{12tt,c}\eta_c) \tag{84}$$

$$\xi_{q,t} = h_t A_t (T_{t,\mathrm{flow}} - T_t)/(w_{34tt,t}\eta_t) \tag{85}$$

Bearing Selection. The heat engine design is linked to the generator design by the shared rotational speed and appropriate bearing selection. While the heat engine subcomponents are not directly affected by the bearing selection, the magnetic field of the generator is greatly influenced by the shaft diameter that results from the selected bearing dimensions. Furthermore, the bearing has great impact beyond component design as it influences rotordynamics, temperature distribution, and system lifetime; this explains why in previous UMGT research, groups have laid their focus on bearing development.

While rotating at extreme speeds of up to 1 million rpm, the UMGT rotor is subjected to both axial and radial loads resulting from aerodynamic and imbalance forces. Despite literature suggesting that roller bearings are not suitable for such conditions and advocating the use of air bearings, the implementation of this approach has proven unsuccessful for various research groups due to failures associated with whirl instabilities, tolerance limitations, and crashes at rigid body modes [1,7,49–52]. In contrast, angular contact bearings offer a compact and ready-to-use solution with a long lifespan and friction losses comparable to air bearings. The achievable speed varies depending on the lubrication method, materials used for the cage, ball, and race, and is defined by the DN-number, describing the tangential speed of the mean bearing diameter
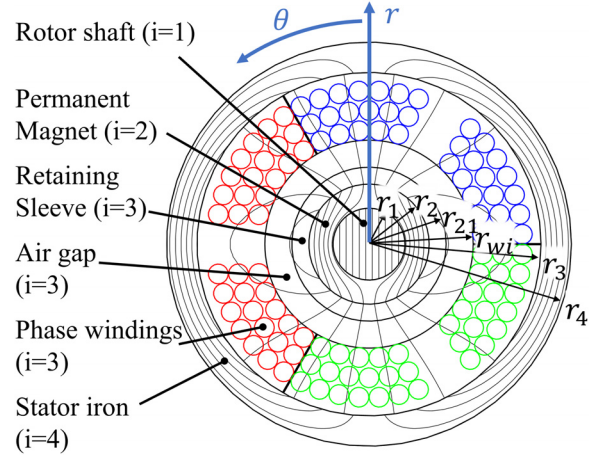

Fig. 7 Axial cross section of slotless generator with magnetic field domains

$$D_m = (D_{b,i} + D_{b,o})/2 \tag{86}$$

$$\mathrm{DN} = \mathrm{rpm}\,D_m \tag{87}$$

For a given rotational speed resulting from the compressor design, it is best practice to opt for bearings rated with higher DN numbers, considering that for the same load they will provide increased lifespan and improved rotordynamic performance. In the scope of this work, open hybrid angular contact bearings with 15° contact angle and dimensions according to diameter series 7 of ISO 15 standard [53] are selected from a bearing manufacturer's catalog (HQW). The selected bearing family has a maximum DN value of 2,400,000 for grease lubrication. The rotor bearing is chosen from the catalog according to the engine rotational speed.

Generator. Following the heat engine component design and bearing selection, the electric generator can be designed as the last component of the UMGT. High-speed permanent magnetic synchronous machines are a popular choice for small motors due to their compact size and high-power density. For speeds above 200,000 rpm, the high frequency magnetic field of the rotor causes excessive eddy current and hysteresis losses in the stator iron. To avoid this effect, a slotless stator iron topology is selected to mitigate magnetic field concentrations, as suggested, for example, by Zwyssig et al. [54]. Furthermore, to minimize magnetic field frequency, a two-pole magnet is used. An axial cross section of this design is depicted in Fig. 7. For the design, the generator shares the rotational system speed with the compressor design. Furthermore, the generator shaft diameter is prescribed by the inner bearing diameter. Beside this, component design is defined by three parameters: Generator design power output $P_{el,\mathrm{design}}$, current density J_{design} and length over diameter ratio ξ_{LD}.

Design Method. Starting the generator design, mechanical and electrical efficiency must be estimated to determine the required electric power output from the system

$$P_{el} = P_{el,\mathrm{design}}/(\eta_g\eta_m) \tag{88}$$

The generator architecture is constrained by the maximum wire temperature, rotordynamics, and stress limits. These three disciplines should be directly controlled by appropriate design variables. In terms of temperature limitations, the area-based current density determines the heat generation in the stator coil due to ohmic losses. As heat transfer from the coil to external heat sinks is proportional to the outer surface area, current density is also a scale independent indicator for the expected coil temperature. Rotordynamics and

stress limits are covered simultaneously by using the generator length over stator iron outer diameter ratio $\xi_{\mathrm{LD}} = L/(2r_4)$.

The electric rotor torque created by the volumetric Lorenz force can be determined as an integral over the coil volume and length [55]

$$T_{el} = \int_0^{l_s} \int_0^{2\pi} \int_{r_{w,i}}^{r_3} r^2 J B_r \, dr d\theta dl \tag{89}$$

Assuming homogeneous magnetic field and phase current in axial direction, the following proportionality can be deduced for the generator design power output:

$$P_{el} \sim \omega T_{el} \sim \omega l_s r^3 J_{\mathrm{design}} B_r \tag{90}$$

Hereby, it can be shown that the effective radial magnetic flux density B_r remains constant if the magnet to stator radius ratio is maintained [56,57]. The proportionalities between power output, rotational speed, shape factor, and machine volume are then determined as follows:

$$P_{el} \sim \omega T_{el} \sim \omega \xi_{LD} r_4^4 J_{\mathrm{design}} \tag{91}$$

$$V \sim \xi_{LD} r_4^3 \tag{92}$$

$$P_{el} \sim V^{\frac{4}{3}} \xi_{LD}^{-\frac{1}{3}} J_{\mathrm{design}} \tag{93}$$

$$V = C_{\mathrm{GV}} \left(\frac{P_{el}}{J_{\mathrm{design}}\omega} \right)^{3/4} \xi_{LD}^{\frac{1}{3}} \tag{94}$$

The external stator iron radius and length can be calculated from the length over diameter ratio parameter ξ_{LD}

$$r_4 = \frac{1}{2} \left(V \cdot \frac{4}{\pi \xi_{\mathrm{LD}}} \right)^{\frac{1}{3}} \tag{95}$$

$$l_s = 2r_4 \xi_{\mathrm{LD}} \tag{96}$$

Together with the radius ratios of magnet and stator iron, the generator volume constant C_{GV} dictates the stator iron field strength. While a stronger stator field results in less current density in the copper windings, the volumetric losses due to hysteresis effects rise. If the field is too weak, the required generator volume and subsequently losses and the weight increase. In the current design, C_{GV} is selected as follows:

$$C_{\mathrm{GV}} = 56 \left[\frac{m^{\frac{9}{4}}}{N^{\frac{3}{4}}} \right] \tag{97}$$

With the facilitated magnet and stator material, the resulting stator iron peak flux density is approximately 0.7 T, presenting a reasonable tradeoff between hysteresis losses, thermal management, and magnet sizing. While stator iron flux density can serve as an additional design parameter, it would introduce an additional subroutine with considerable computational effort to adjust the radius ratios until the required magnetic field is achieved. Instead, the following geometric ratios are implemented, yielding the required flux density when using a Sm2Co17 magnet:

$$r_2 = 0.145(r_4 - r_1) + r_1 \tag{98}$$

$$t_{\mathrm{ag}} = 0.5 \, \mathrm{mm} \tag{99}$$

$$r_{21} = r_2 + t_s \tag{100}$$

$$r_{wi} = r_{21} + t_{\mathrm{ag}} \tag{101}$$

$$t_{si} = 0.15 \cdot r_4 \tag{102}$$

$$r_3 = r_4 - t_{si} \tag{103}$$

Hereby, the internal shaft radius r_1 is given from the bearing selection. The titanium sleeve thickness t_s is determined in a separate subroutine to preserve required stress limits of the permanent magnet.

Due to the high tangential speed, the generator permanent magnet needs to be contained by a press-fitted titanium sleeve. The differential equation for the radial displacement u for a rotating disk at any radius r is given as [58]

$$\frac{E}{1-\nu^2} \left(r^2 \frac{\partial^2 u}{\partial r^2} + r \frac{\partial u}{\partial r} - u \right) = \rho r^3 \omega^2 \tag{104}$$

The boundary and interface conditions for rotating disk assemblies are well known, as also described in Ref. [59]. In the current model, the permanent magnet and titanium sleeve are treated separately from the shaft, as the adhesive connecting magnet and shaft has negligible stiffness. The boundary condition at the inner radius of the magnet is then given by $\sigma_{r,ri,m} = 0$. Together with elasticity relations, the radial and tangential stresses can be derived for given sleeve thickness t_s and radial interference between the sleeve and the magnet, if_s. The maximum directional von Mises stress occurs at the inner radii of magnet and sleeve

$$\sigma_{ri} = \sqrt{\sigma_{r,ri}^2 + \sigma_{t,ri}^2 - \sigma_{r,ri}\sigma_{t,ri}} \tag{105}$$

The resulting sleeve and magnet stresses must be smaller or equal to the yield strength divided by the respective safety factor

$$\sigma_{m,\mathrm{max}} \leq \frac{\sigma_{m,\mathrm{yield}}}{S_m}, \quad \sigma_{s,\mathrm{max}} \leq \frac{\sigma_{s,\mathrm{yield}}}{S_s} \tag{106}$$

Hereby, the maximum stress always occurs at the inner radius [58]. Consequently, the sleeve thickness is minimized by reducing the difference between the permissible stress and the inner radius stress for both components, magnet and sleeve, simultaneously. This can be achieved by defining the Euclidian stress distance $\Delta\sigma$

$$\Delta\sigma(t_s, if_s) = \sqrt{(\sigma_{m,ri} - \sigma_{m,\mathrm{max}})^2 + (\sigma_{s,ri} - \sigma_{s,\mathrm{max}})^2} \tag{107}$$

If the Euclidian stress distance is zero, the stresses at magnet and sleeve inner radius correspond exactly to the respective material limits and the minimum sleeve thickness is found. To this end, a minimization routine is applied for $\Delta\sigma(t_s, if_s)$

$$\min \Delta\sigma(t_s, if_s) \tag{108}$$

Using the MATLAB function fminsearch starting from an initial guess for t_s and if_s, the Euclidian stress distance is automatically reduced, yielding the minimum achievable sleeve thickness while maintaining structural integrity. An exemplary minimization path is depicted in Fig. 8. The selected safety factors for the Samarium Cobalt magnet and titanium sleeve are set to 1.5 and 1.2, respectively.

With all dimensions and material properties defined, the resulting current density can be determined analytically owing to the simple geometry of the slotless stator iron topology. Here, the calculated current density can deviate from the design value due to varying sleeve thickness depending on the stress calculation as presented earlier. The procedure used in this effort is based on the analysis of Polinder [60], with simplifications considering the magnetic field generated by the phase coils (armature field) to be negligible compared to that of the permanent magnet, and the magnetic field to be axially uniform (neglecting 3-D effects). These assumptions have been validated both numerically and experimentally [61].

The magnetic flux density $\boldsymbol{B}$ is a conservative vector field resulting from the gradient of a scalar potential A, which means $\boldsymbol{B}$
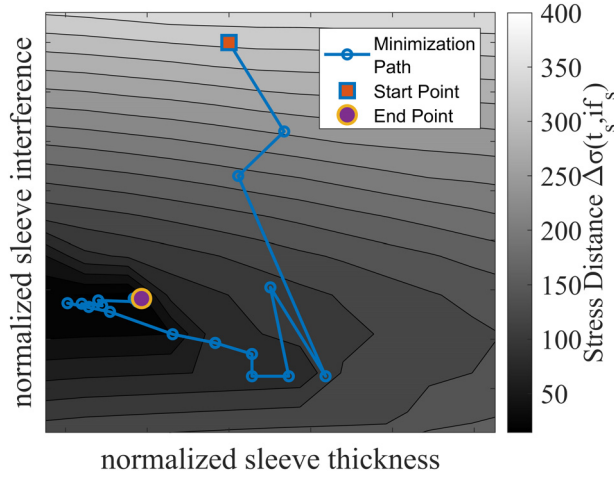
Fig. 8 Finding minimum achievable sleeve thickness by minimization of the Euclidean stress distance

must fulfill magnetic flux continuity. When the effect of the armature field created by the coil current density J is neglected, this leads to the Laplace equation in the polar coordinates (for coordinate convention, see Fig. 7)

$$\nabla^2 A = -\nabla \times \boldsymbol{B} = 0 \tag{109}$$

$$\frac{\partial^2 A}{\partial r^2} + \frac{1}{r}\frac{\partial A}{\partial r} + \frac{1}{r^2}\frac{\partial^2 A}{\partial \theta^2} = 0 \tag{110}$$

The solution for the scalar potential in each region of the generator (denoted by i, see Fig. 7) can be written as follows [61]:

$$A_i = -\left(C_i r + \frac{D_i}{r}\right)\cos(\theta_r) \tag{111}$$

The magnetic flux density vector field is found from $\boldsymbol{B} = \nabla A$

$$\boldsymbol{B}_i = \left(\left(C_i + \frac{D_i}{r^2}\right)\sin(\theta_r), \left(C_i - \frac{D_i}{r^2}\right)\cos(\theta_r)\right) \tag{112}$$

As the armature field is neglected, the magnetic field intensity is determined from the magnetic flux density and respective permeability

$$\boldsymbol{H}_i = \boldsymbol{B}_i / \mu_i \tag{113}$$

Then, the system of equations for all generator regions is closed by the following interface and boundary conditions [60,61]: the magnet is diametrically magnetized, $D_1 = 0$; through magnetic flux continuity, the radial flux density component must be equal at the interface of the two domains, $B_{i,r}(r = r_i) = B_{i+1,r}(r = r_i)$; through Ampere's continuity condition, the azimuthal field intensity component of adjacent regions must be conserved $H_{i,\theta}(r = r_i) = H_{i+1,\theta}(r = r_i)$; and no magnetic field exists outside the stator iron, $B_{4,r}(r = r_4) = 0$

A determined system of seven equations is solved for regions i equal to 1–4, yielding all the C_i and D_i constants to determine the scalar potentials A_i and magnetic flux density vector fields $\boldsymbol{B}_i$. For the calculation of current density, only the scalar potential of the coil area ($i = 3$) is relevant. First, the effective phase voltage can be found directly from the vector potential at the mean phase winding radius $r_{wm} = (r_{wi} + r_3)/2$, according to Ref. [61]

$$e_{\text{eff}} = \frac{1}{\sqrt{2}}\left|\frac{6}{\pi}\omega N l_m A_3(r_{wm})\right| \tag{114}$$

The rotor torque resulting from a given current is diminished for concentrated windings with 120 deg spacing (compared to windings

with 180 deg spacing). To achieve the required electric power output, the effective phase current is calculated from the induced voltage using a winding factor f_w [62]

$$i_{\text{eff}} = P_{el}/(3f_w e_{\text{eff}}), f_w = 0.87 \tag{115}$$

Due to the high rotation frequencies anticipated in this application, it is necessary to use strand-wise insulated litz wire for the coil windings, reducing skin effect losses. The resultant copper current density can be approximated using correction factors for coil winding and litz strand packaging density $f_{p,\text{coil}}$ and $f_{p,\text{litz}}$, respectively

$$A_{\text{cu}} = f_{p,\text{coil}} f_{p,\text{litz}} \pi \left(r_3^2 - r_{wi}^2\right)/(6N) \tag{116}$$

$$J_{\text{calc}} = A_{\text{cu}}/i_{\text{eff}} \tag{117}$$

It should be noted that current density is independent of the number of turns N, which is canceled out if Eq. (117) is substituted by Eqs. (114)–(116). Therefore, N is a free parameter that is merely used to tune the phase voltage and current to the available converter topology once an optimum engine design is found.

Performance Model. Toward optimizing system performance with accurate modeling of the thermal behavior, it is important to estimate the generator losses, which can be divided into copper, stator iron, and air friction losses. According to Refs. [57,61], the skin effect and winding eddy current losses can be neglected if a litz diameter of 0.1 mm is used. Hence, the copper loss consists merely of the DC phase losses

$$P_{\text{cu,DC}} = 3 \cdot i_{\text{eff}}^2 R_{\text{DC,phase}} \tag{118}$$

$$R_{\text{DC,phase}} = \rho_{\text{cu}} l_{\text{Cu}}/A_{\text{cu}} \tag{119}$$

$$l_{\text{cu}} = 2N l_m (r_3 - r_{wi}) \tag{120}$$

It can be shown by substituting Eq. (118) with (119), (116), and (115) that copper losses are merely a function of current density independent of N. Hysteresis and eddy current effects cause stator iron losses, which can be modeled using the Steinmetz equation [61]:

$$P_{\text{Iron}} = k_{si} \cdot f^\alpha \cdot B_{si,\text{eq}}^\beta \cdot V_{si} \tag{121}$$

Hereby, k_{si}, α, and β are used according to material properties for silicon iron laminations with 168 μm thickness, as reported in Ref. [57].

In addition, the air friction between rotor and stator contributes significantly to the overall generator losses and can be calculated as follows:

$$P_{f,\text{air}} = c_f \pi \rho_{ag} \omega^3 r_{21}^4 l_{ag} \tag{122}$$

The friction coefficient c_f is calculated based on the gap flow regime. As can be derived from linear stability analysis [63], vortex structures occur for Taylor numbers $\text{Ta} = \omega r_{21} t_{ag}\sqrt{t_{ag}/r_{21}}/\nu$ above the critical value of 41.2 while the gap flow is fully turbulent for $\text{Ta} > 400$. Owing to the high tangential velocities required for microturbine generators, only turbulent conditions need to be considered. For this case, a single flow regime with linear scaling of the friction coefficient with $\text{Ta}^{0.2}$ starting from the onset of instability is suggested [64]

$$\text{Re}_{ag,\text{cr}} = 41.2/\sqrt{t_{ag}/r_{21}} \tag{123}$$

$$c_{f,\text{cr}} = \frac{1.8}{\text{Re}_{\text{cr}}} \frac{(r_{21} + t_{ag})^2}{(r_{21} + t_{ag})^2 - r_{21}} \left(\frac{t_{ag}}{r_{21}}\right)^{-0.25} \tag{124}$$

$$C_0 = c_{f,\text{cr}}/41.2^{-0.2} \tag{125}$$

$$c_{f,\text{Mack}} = C_0 \text{Ta}^{-0.2} \tag{126}$$

Tested with high-speed motors to Taylor numbers of up to 1400, this correlation is shown to have a good agreement with experiments [65]. An alternative calculation based on the gap Reynolds number $\text{Re}_g = r_{21}^2 \omega/\nu$ was suggested by Bilgen and Boulos [63], who evaluate the turbulent friction factor based on two regimes

$$c_{f,\text{Bilgen,Re}\leq 10^4} = 0.515 \left(t_{\text{ag}}/r_{21}\right)^{0.3}/\text{Re}_{\text{ag}}^{0.5} \tag{127}$$

$$c_{f,\text{Bilgen,Re}>10^4} = 0.0325 \left(t_{\text{ag}}/r_{21}\right)^{0.3}/\text{Re}_{\text{ag}}^{0.2} \tag{128}$$

The equations are a best-fit to a broad set of experimental data with Reynolds numbers up to 10^6. Since the losses estimated by the two models is observed to vary by up 300%, as a less biased indicator, it is decided to average the two friction factor predictions, yielding

$$c_f = (c_{f,\text{Mack}} + c_{f,\text{Bilgen}})/2 \tag{129}$$

Model Validation

In the previous sections, an automated conceptual design strategy integrating all subcomponents necessary to form a functional UMGT has been described. In a second step, the numerical and experimental validation of the proposed reduced order performance models is presented.

Compressor Model Computational Fluid Dynamics Validation. The reduced order compressor model has been established based on semi-empirical loss models, stemming predominantly from experience in large-scale compressors. Therefore, it is necessary to validate it for small-scale machines, capturing at least the general trends required to be used in system optimization. Nowadays, RANS CFD simulations are commonly used for radial compressor performance prediction in various applications, such as industrial compressors, turbochargers, and microgas turbines [66–68]. As a relatively higher fidelity validation tool, three-dimensional RANS CFD simulations are conducted to contrast with the reduced order model estimates.

To this end, geometries of different compressor stages are generated. The design mass flowrate and rotor total pressure ratio of each stage are set to 5.2 g/s and 2.8, respectively. These values are chosen based on a previous thermodynamic cycle analysis for a 300 W scale gas turbine [7,39]. The flow and work coefficient are varied between 0.02 to 0.08 and 0.5 to 0.9 respectively with 6 evaluation levels, resulting in 36 different compressor stages. The compressor inducer hub to shroud ratio is constant at 0.3 for all designs while rotational speed of each rotor is defined from the global flow coefficient according to Eq. (7). Tip clearance and blade thicknesses are adjusted, corresponding to the design model according to Eqs. (15) and (16). In the scope of the comparison, roughness effects are neglected, and smooth compressor surface is assumed. Moreover, disk friction losses are excluded. The resulting 36 stage geometries are subsequently simulated through RANS CFD in ANSYS CFX framework using the standard shear-stress transport k-omega turbulence model, which has shown good agreement with experimental data of small-scale radial compressors [69].

The simulation of each compressor stage involves a single rotating domain containing the radial inlet section, rotor, and vaneless diffuser, with no need for a rotor–stator interface. The rotor's tip clearance is adjusted, and inlet total temperature and total pressure as well as outlet mass flow and rotational speed are prescribed as boundary conditions for each stage design. The rotor geometry is treated with smooth and adiabatic walls. A mesh refinement study is conducted, revealing that the CFD predictions of pressure ratio and efficiency reach a satisfactory level of grid independence at around 470 k structured elements. The convergence of the simulations is assumed once stage efficiency standard variation of the last 10 iterations reaches less than 0.05%.

Based on the reduced order model and the RANS CFD simulations, the resulting Smith charts of all 36 compressor stages are depicted in Fig. 9. The efficiency evaluation shows good agreement between CFD and one-dimensional (1D) model, predicting an optimum region for flow and work coefficients around 0.05 and 0.6, respectively. The optimum flow coefficient of both analysis methods is shifted to lower values compared to a nominal value of 0.07, as often stated in literature such as in Ref. [13]. This is in part because relative blade thickness increases at high flow coefficients due to manufacturing limitations, resulting in increased relative Mach numbers, profile losses, and higher sensitivity to incidence. However, there is also a bias in the analysis considering that disk friction losses are not captured in neither the reduced order model nor the CFD as the backplate gap is not integrated in the numerical setup. Therefore, in the scope of the comparison, the stage designs with low flow coefficients are not penalized by higher disk friction that degrades the efficiency.

Nevertheless, the reduced order model compares well with general trends of the CFD. At high work coefficients, tip clearance and blade loading losses rise owing to higher pressure difference between suction and pressure sides, and higher relative velocity level. Moreover, the friction losses are more pronounced in the
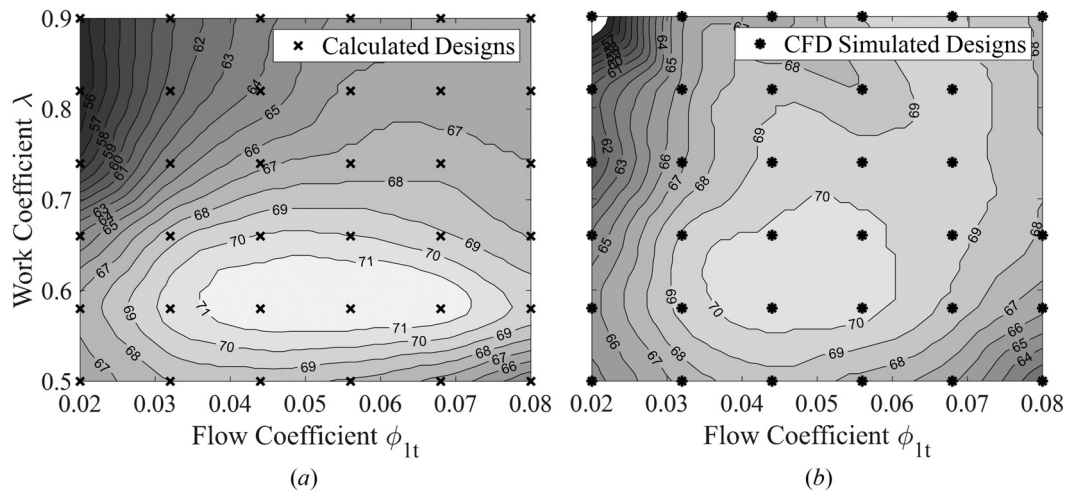

Fig. 9 1D model prediction (*a*) and CFD results (*b*) of polytropic total to total stage efficiency for 36 compressor stages
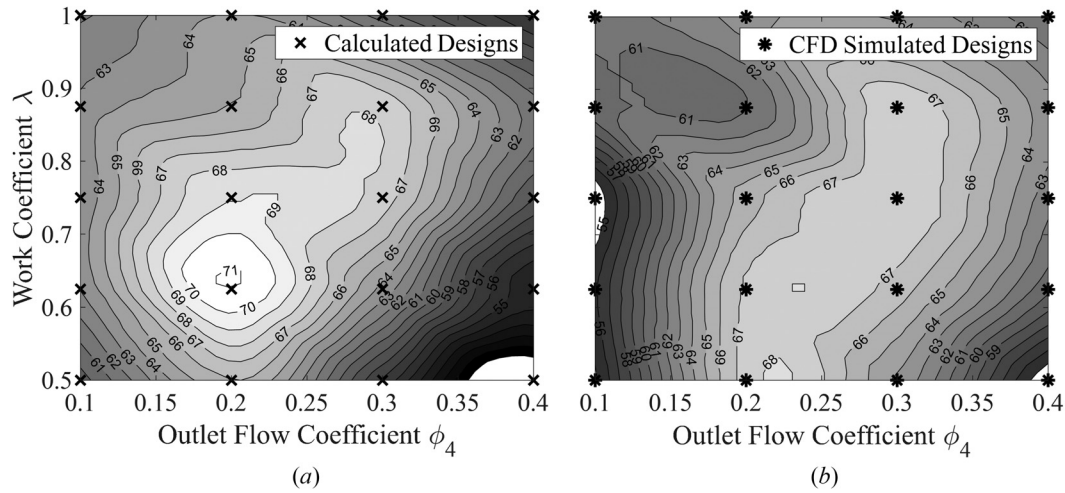
Fig. 10 1D model prediction (*a*) and CFD results (*b*) of polytropic total to static stage efficiency for 20 turbine stages
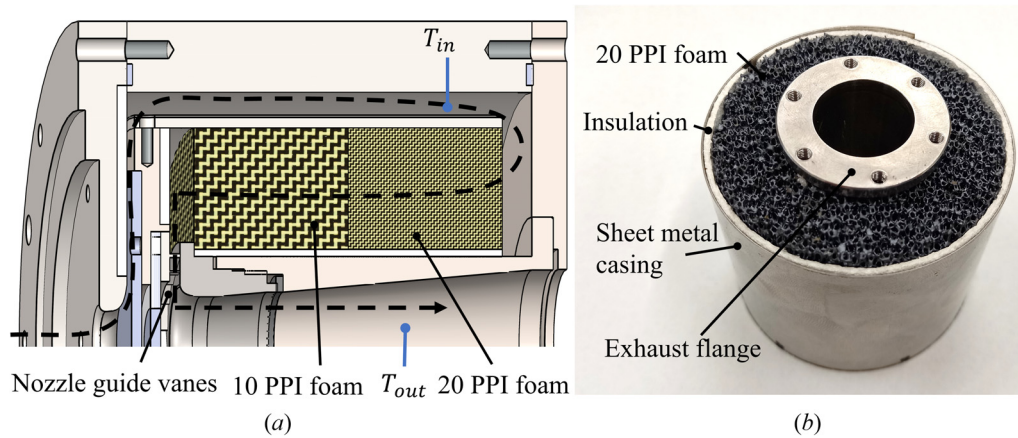

Fig. 11 Reverse flow combustor prototype assembly including two-stepped ceramic foam (*a*), insulated ceramic foams contained by sheet metal casing (*b*)

corners of the Smith chart due to narrow flow passages for low flow coefficients and higher velocity levels at high work coefficients. The comparison between reduced order model and CFD has been repeated for 25 additional compressor stages with a pressure ratio of 2.2 at a flowrate of 10 g/s (not shown here), representing lower tip speed designs. The findings reflect a similar level of consistency, building confidence that the 1D compressor stage model provides sufficiently accurate performance predictions.

Turbine Model Computational Fluid Dynamics Validation. To validate the turbine performance modeling procedure, multiple stages are generated with a design speed of 500,000 rpm, flowrate of 5.2 g/s and total inlet temperature and pressure of 1200 K and 2.5 bar, respectively. Yielding 20 different configurations, the flow and loading coefficients are used as input parameters ranging from 0.1 to 0.4 and from 0.5 to 1, respectively. Subsequently, the reduced order performance evaluation is conducted for each stage, excluding disk friction losses. To corroborate the findings numerically, the stage gas paths are then discretized following a refinement study using structured meshing with approximately 350 k elements for the rotor and 200 k elements for the stator. Total temperature and pressure as well as flow angle are prescribed as inlet boundary conditions to the guide vanes while a static pressure boundary is applied at the rotor exit. All walls are treated as adiabatic and smooth. For the domain coupling of rotor and stator, a mixing plane

interface is selected. RANS simulations are conducted in ANSYS CFX using the standard shear-stress transport k-omega turbulence model.

The resulting Smith-charts for the 1D model and CFD results are charted in Figs. 10(*a*) and 10(*b*), respectively. Both models predict a region of high efficiency for flow coefficients between 0.15 and 0.3 and work coefficients between 0.65 and 0.9. This is in line with stage efficiency trends observed in literature, indicating a peak in this region [35,38,42]. Outside this region, efficiency drops for lower and higher outlet flow coefficients, which can be explained by the increased stator and passage losses, respectively. Due to augmented pressure difference and reduced blade height, tip clearance effects become more pronounced for high flow coefficients in combination with high work coefficients. When comparing 1D and CFD performance calculation, the 1D model overpredicts stage efficiency by 2–3%. Moreover, the 1D model predicts a more distinct optimum at a work coefficient around 0.65, which is not present in the CFD results. Nevertheless, generally reasonable agreement is observed between the efficiency predictions of the 1D model and the CFD.

Combustor Model Experimental Validation. In order to substantiate the combustor model empirically, a prototype combustor test rig with a reverse flow burner is developed, consisting of two axially stacked silicon carbide foam annuli. Figure 11 shows a photograph of the combustor core and a cross section of the test rig

Table 1 Ceramic foam specifications

Material	Silicon carbide
Cell sizes	10 PPI, 20 PPI
Porosity	88%
Topology	Unstructured
Density	2900 kg/m^3 (solid)
Heat capacity	700 J/kg-K (solid)
Heat conductivity	110 (RT), 45 W/m-K (1000 °C)
Thermal emissivity	0.8 [70]

assembly. Detailed foam specifications provided by the manufacturer are given in Table 1.

By using a 20 PPI cell size foam at the burner entry, heat transfer to the incoming reactants is improved and flashback is prevented while the coarse 10 PPI foam serves as the reaction zone. A 1.5-mm zirconia insulation sheet minimizes the conductive heat losses at both the outer and inner radii. The insulated ceramic foams are placed in a stainless-steel casing. In the current test setup, the combustor is operated with propane–air mixture and the equivalence ratio is between 0.45 and 0.6, by controlling the fuel flow at constant air flowrate. Once steady-state conditions are reached, inlet and exhaust temperatures are measured with K-type thermocouples at locations depicted in Fig. 11. The estimated exhaust temperature measurement uncertainty exceeds 20 K due to radiative bias and the known presence of temperature variation. Nevertheless, to evaluate the magnitude of heat loss, measurements are recorded at 1 g/s and 1.5 g/s air mass flow rates.

The experimental results are depicted in Fig. 12 in terms of outlet gas temperature with respect to equivalence ratio. Expectedly, the outlet temperature of the combustor increased for rich mixtures, but the measured values are consistently lower than calculated adiabatic flame temperatures according to Ref. [71]. Additionally, increasing flowrate at a given equivalence ratio significantly increases combustor outlet temperature, suggesting relatively high heat transfer losses being the source of the poor combustor efficiency. If low chemical efficiency were the source of the below-adiabatic flame temperature readings from the outlet thermocouple, increasing mass flowrate would rather be expected to further reduce the temperature readings owing to decreased residence time. Moreover, it is known that data from small-scale gaseous combustors with similar reaction time showed chemical efficiencies above 99% [23]. When comparing the experimental observations with the presented heat loss model relying on radiative and convective heat transfer, the measured temperatures present good agreement for both flow rates, corroborating the reduced order model calculation. Hereby, calculated convection heat losses exceed radiative heat losses at
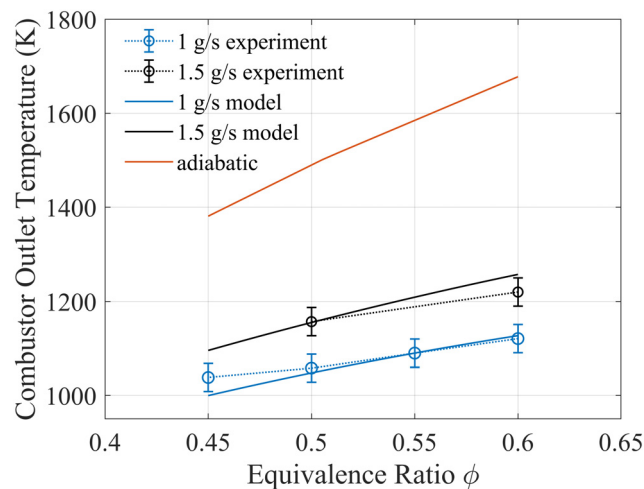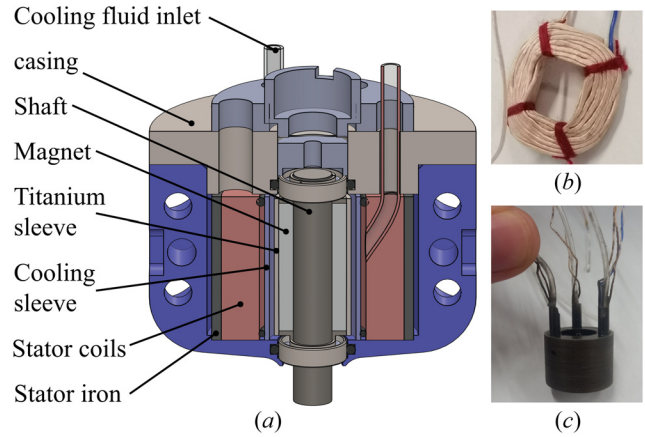
Fig. 13 Prototype generator topology (*a*), 120 deg phase coil with 50 windings (*b*), and potted phase coils with cooling tubes (*c*)

Table 2 Prototype generator dimensions

r_1 (mm)	r_2 (mm)	r_{wi} (mm)	r_3 (mm)	r_4 (mm)	l_m (mm)
2	3.5	5.5	8.5	10.5	14.8

low temperatures, while at exhaust temperature above 1220 K, radiative heat losses become dominant.

Generator Model Experimental Validation. Toward comparison with the phase voltage and air friction loss models, a prototype 2-pole, 3-phase motor-generator is developed with concentrated windings ($N = 50$) and an internal cooling system, Fig. 13. The phase coils are manufactured manually and pressed into defined geometrical shapes to ensure 120 deg phase spacing. The magnet material is selected as Sm2Co17 grade M32, due to its high temperature capabilities. All electric machine dimensions are documented in Table 2. Suspended on O-rings to allow bearing alignment at high speeds, open angular contact bearings with ceramic balls and grease lubrication are used and shielding is achieved by tight casing clearances at the axial bearing ends. The bearing dimensions follow diameter series 7 of ISO 15 standard [21] with internal and external diameters of 4 mm and 7 mm, respectively, at an axial length of 2 mm and ball diameter of 1 mm. The rotor is balanced in two planes to a precision of 2 mg-mm.

Using a digital oscilloscope, the no-load voltage is measured at 50,000 rpm by driving the rotor spindle with a coupled air turbine. Depicted in Fig. 14(*a*), the modeled and measured phase voltage are found to be in good agreement, validating the magnetic field calculation. Moreover, air friction losses can be determined by conducting runout tests in ambient conditions and in a vacuum chamber at 60 mbar. The rotor losses are then calculated from the angular deceleration and the rotor moment of inertia for each data point

$$P_{\text{loss}}(\omega) = \omega \frac{d\omega}{dt} I_{\text{rotor}} \qquad (130)$$

The air friction loss curve is given by the difference between losses at ambient pressure and vacuum

$$P_{f,\text{air}}(\omega) = P_{\text{loss,amb}}(\omega) - P_{\text{loss,vac}}(\omega) \qquad (131)$$

Comparing the measured air friction losses with the models suggested by Mack and by Bilgen and Boulos, Fig. 14(*b*) shows that the experimental observations lie in between two bounds of the predictions, and the averaging the two estimates provides reasonable agreement with the empirical data.
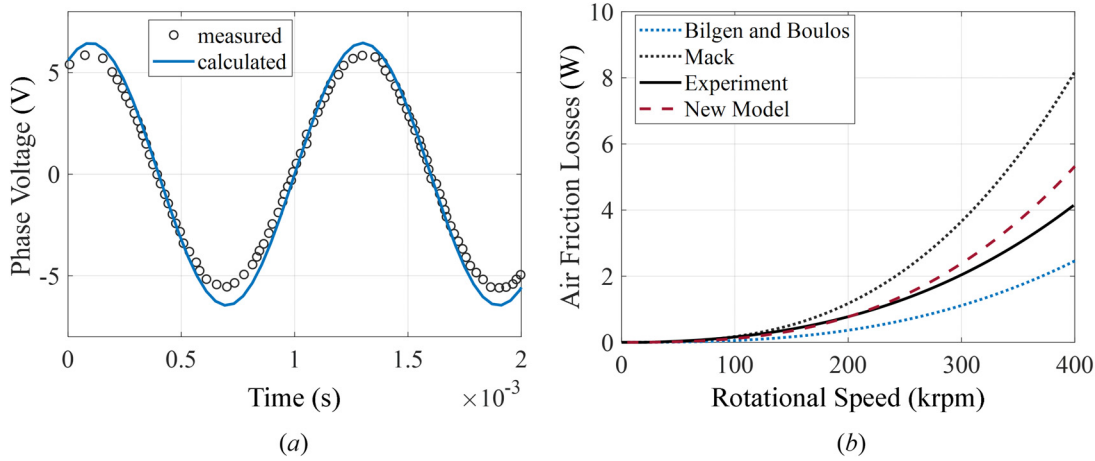

Fig. 12 Measured and modeled combustor exhaust temperature with and without considering heat losses

Fig. 14 phase voltage measurement and model (*a*) and air friction loss models and experimental results (*b*)

Discussion

In the previous sections, a coherent component design strategy with numerically and experimentally validated performance models is elaborated. Figure 15 summarizes the heat engine and generator design process highlighting all submodules, input parameters, and exchange of information.
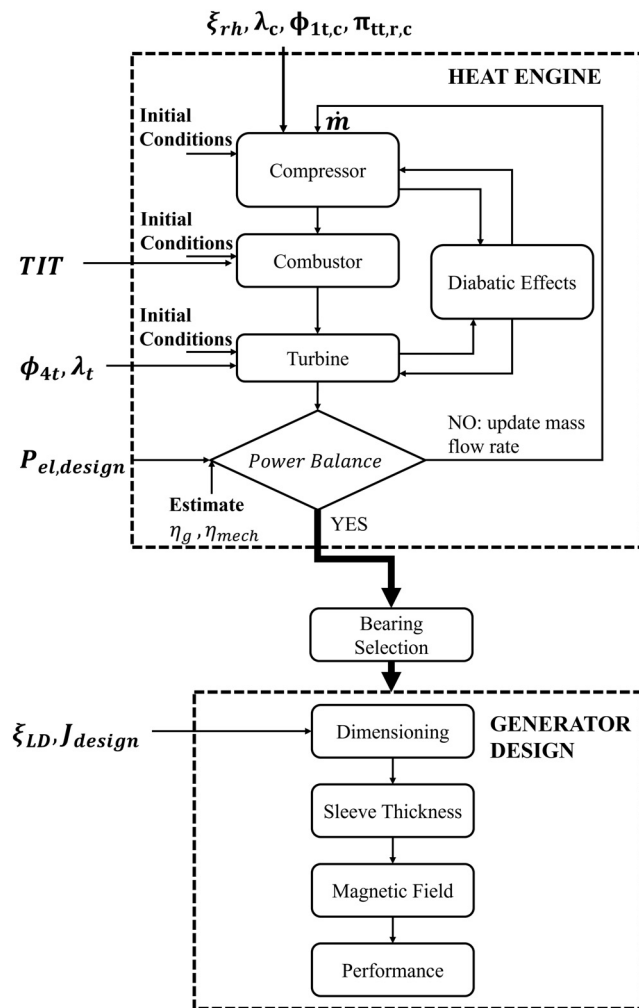

Fig. 15 Integrated component design framework using the presented reduced order models

To initiate the heat engine design, a preliminary guess for the heat engine mass flowrate is required. Subsequently, compressor design and rotor speed are calculated iteratively based on four free input parameters while continuously updating performance prediction according to the implemented loss models. Using the system mass flowrate as well as calculated compressor outlet temperature and pressure, the combustor geometry is defined, and pressure drop and heat losses are determined iteratively for given TIT. Subsequently, facilitating combustor exit parameters and using system rotational speed and flowrate as well as two further design variables, the radial turbine stage is designed and assessed iteratively. Once the design and performance calculations converge, the resulting system power output resulting from compressor and turbine work can be determined based on the initial system mass flowrate, generator and mechanical efficiency

$$\dot{m} = P_{el,\text{design}} / \left[(w_c - w_t)(\eta_g \eta_m) \right] \qquad (132)$$

The updated system mass flow is then used for the next heat engine design iteration until a minimum residual of 1×10^{-4} is reached. Once the heat engine calculation converged, the rotational speed is given and a high-speed bearing with respective shaft diameter as well as axial and radial loading coefficients is selected from a manufacturer catalog (HQW).

Based on the required electric power output, rotational speed, and shaft diameter, the generator design is initiated using two further design parameters. To this end, the magnet radius is calculated and subsequently the required sleeve thickness is determined according to the outlined minimization method such that magnet and sleeve stresses are as close to their respective material limits as possible. Now, the radii of the windings and stator iron are calculated and the required current density is found based on the resulting magnetic flux density. Finally, all parameters are passed on to the described loss models and the generator efficiency is determined.

The proposed methodology enables quick automated component design using just ten input parameters, making it ideal for design space exploration. On average, the computation time for one conceptual UMGT design is 0.4 CPU seconds on a modern Xeon Core. In contrast, previous literature often saw component topologies and specifications chosen manually or with the assistance of various software packages because of the absence of an automated calculation strategy.

It's important to note that this paper focuses solely on component-level design and evaluation. Subsequent steps involve integrating these components into a conceptual system layout by defining the UMGT rotor and casing geometry. Following this, system performance, including efficiency, bearing lifetime, heat transfer, rotordynamics, and stress analysis, should be evaluated; these steps are covered in Part II of this work.

Conclusion

A reduced order design and analysis method is elaborated for ultramicrogas turbines with power output in the 1000 W order. Hereby, a coherent design framework is presented merging compressor, turbine, combustor, and generator by considering effective design parameters and matching conditions. In addition, reduced order performance models are presented for all components. Compressor and turbine losses are compiled from existing literature sources and adapted by modifying parameters to reflect small-scale effects. A new heat loss model for the porous media combustor is developed considering radiation as the main contributor to performance degradation. Additionally, various loss sources of the electric generator are highlighted, and two different air friction models are compared.

Following component design and performance modeling, the reduced order models are validated using higher fidelity numerical and experimental data. CFD results of multiple compressor and turbine stages are compared to the reduced order models, showing reasonable quantitative agreement, as well as capturing the general trends. Additionally, the combustor heat loss model is shown to match with measurement results of a prototype combustor operated at various mass flow rates and equivalence ratios. Finally, air friction loss measurements on a high-speed generator prototype reflected the good agreement to the average of two winding loss models existing in literature.

In conclusion, the present work demonstrates an experimentally validated ultramicrogas turbine generator design framework, utilizing only ten input variables to fully define all system components. By this integrated approach, interdependencies of components are inherently considered resulting in a truly multi-disciplinary conceptual design strategy. Furthermore, using a set of reduced order models instead of higher-fidelity computation allows rapid evaluation of multiple configurations in short time, thus encouraging design space exploration and system optimization prior to detailed engineering. In Part II, the component design is merged into a system layout and subsequently analyzed using reduced order models for rotordynamics, stresses, bearing lifetime and system efficiency. In the following, constrained multi-objective optimizations of 300 W gas turbine is demonstrated, proposing optimum design parameters for small-scale generators depending on their rotor material.

Data Availability Statement

The datasets generated and supporting the findings of this article are obtainable from the corresponding author upon reasonable request.

Nomenclature

Latin Symbols

A = area (m^2)/magnetic field scalar potential
b = blade height (m)
B = flow blockage
B = magnetic flux density (T)
c = absolute velocity (m/s), thermal conductance (W/m)
c_f = friction coefficient
C_{GV} = generator volume constant $\left(\frac{\text{m}^{\frac{9}{4}}}{\text{N}^{\frac{3}{4}}}\right)$
c_p = heat capacity at constant pressure (J/(kg K))
Da = Damköhler number
DH = De Haller number
D_m = mean bearing diameter (m)
DN = bearing diameter-speed number (m/min)
e = tip clearance (m)/phase voltage (V)
E = Young's modulus (Pa)
f = frequency (Hz)
f_p = packaging factor
f_w = winding factor
h = specific enthalpy (J/kg), heat transfer coefficient $(\text{W}/(\text{m}^2\text{K}))$
i = incidence angle (deg), phase current (A)
if = interference (m)
J = current density (A/m^2)
k = proportionality factor/thermal conductivity (W/(mK))
l = length (m)
LHV = lower heating value (J/kg)
M = Mach number
$\dot{m}$ = mass flow rate (kg/s)
n = polytropic exponent
N = number of windings
o = throat width (m)
P = pressure (Pa)/power (W)
q = specific heat flux (J/kg)
Q = heat flux (W)
r = radius (m)
R = gas constant (J/(kg K))
Re = Reynolds number
rpm = rotations per minute
S = stress safety factor
Ta = Taylor number
t = thickness (m)
t_b = blade thickness
T = temperature (K)
TIT = turbine inlet temperature (K)
u = circumferential velocity (m/s), radial displacement (m)
V = volume (m^3)
w = specific technical work (J/kg), relative velocity (m/s)
W = normalized relative velocity
x = flow path length (m)
Z = number of blades

Superscript

′ = relative frame of reference condition

Greek Symbols

α = absolute flow angle (deg)
β = blade angle/relative flow angle with respect to meridional coordinate (deg)
γ = ratio of specific heats

ϵ = emissivity, turbine expansion ratio
η = efficiency
λ = work coefficient
μ = dynamic viscosity (Pa s)/permeability (N/A^2)
ν = kinematic viscosity (J s/kg)/Poisson ratio
ξ_{cms} = meridional velocity ratio
ξ_{LD} = length over diameter ratio
ξ_q = diabatic heat ratio
ξ_{rh} = compressor hub radius ratio
ξ_{rs} = tip radius ratio
π = pressure ratio
ρ = density (kg/m^3)
σ = slip factor, Stefan–Boltzmann constant (W/(m^{2}K^4)), stress (MPa)
τ_{chem} = chemical reaction time (s)
τ_{res} = residence time (s)
ϕ = flow coefficient, equivalence ratio
ω = angular velocity (rad/s)

Subscripts

ag = airgap
amb = ambient
as = after shock
b = blade
bi = inner bearing radius
bs = before shock
c = compressor
cc = combustion chamber
chem = chemical combustion efficiency
cl = clearance/clearance loss
cr = critical
cu = copper
DC = direct current
eff = effective
el = electrical
g = generator
h = hub
i = incidence, inner
id = ideal
im = intermediate shaft between compressor and turbine
l = loss
m = meridional/mechanical/metal blockage/magnet
max = maximum
n = nozzle
o = outer
p = passage loss
r = rotor, radial
rad = radiation
re = recirculation loss
ri = inner radius
s = shroud condition/generator stator/sleeve
si = stator iron
t = total condition/tangential direction
te = trailing edge/trailing edge loss
u = circumferential direction
vac = vacuum
vd = vaneless diffuser
wi = winding inner radius
wm = mean phase winding radius
x = flow path length
1 = compressor inlet/turbine guide vane leading edge/generator shaft radius
2 = compressor rotor outlet/turbine guide vane trailing edge/magnet outer radius
21 = titanium sleeve outer radius
3 = compressor diffuser inlet/turbine rotor inlet/stator iron inner radius
4 = compressor diffuser outlet/turbine rotor outlet/stator iron outer radius

References

[1] Epstein, A. H., 2004, "Millimeter-Scale, Micro-Electro-Mechanical Systems Gas Turbine Engines," ASME J. Eng. Gas Turbines Power, **126**(2), pp. 205–226.

[2] Mehra, A., 1997, "Computational Investigation and Design of Low Reynolds Number Micro-Turbomachinery," Master thesis, Department of Aeronautics and Astronautics, Massachusetts Institute of Technology, Cambridge, MA.

[3] Gong, Y., Sirakov, B. T., Epstein, A. H., and Tan, C. S., "Aerothermodynamics of Micro-Turbomachinery," ASME Paper No. GT2004-53877.

[4] Fréchette, L. G., Jacobson, S. A., Breuer, K. S., Ehrich, F., Ghodssi, R., Khanna, R., Wong, C. W., Zhang, X., Schmidt, A., and Epstein, A. H., 2000, "Demonstration of a Microfabricated High-Speed Turbine Supported on Gas Bearings," Research Report of the Gas Turbine Laboratory and Microsystems Technology Laboratories, Massachusetts Institute of Technology, Report No. 0704-0188.

[5] Ishihama, M., Sakai, Y., Matsuzuki, K., and Hikone, T., 2003, "Structural Analysis of Rotating Parts of an Ultra Micro Gas Turbine," Proceedings of the International Gas Turbine Congress, Tokyo, Japan, Nov. 2–7, pp. 1–4.

[6] Epstein, A. H., Jacobson, S. A., Protz, J. M., and Frechette, L. G., 2000, "Shirtbutton-Sized Gas Turbines: The Engineering Challenges of Micro High Speed Rotating Machinery," Proceedings of the 8th International Symposium on Transport Phenomena and Dynamics of Rotating Machinery, Honolulu, Mar. 26–30, pp. 26–30.

[7] Badum, L., Leizeronok, B., and Cukurel, B., 2021, "New Insights From Conceptual Design of an Additive Manufactured 300 W Micro Gas Turbine Towards UAV Applications," ASME J. Eng. Gas Turbines Power, **143**(2), p. 021006.

[8] Lake, T., Stokes, J., Murphy, R., Osborne, R., and Schamel, A., 2004, "Turbocharging Concepts for Downsized DI Gasoline Engines," SAE Paper No. 2004-01-0036.

[9] Tanaka, S., Isomura, K., Togo, S. I., and Esashi, M., 2004, "Turbo Test Rig With Hydroinertia Air Bearings for a Palmtop Gas Turbine," J. Micromech. Microeng., **14**(11), pp. 1449–1454.

[10] Dessornes, O., Landais, S., Valle, R., Fourmaux, A., Burguburu, S., Zwyssig, C., and Kozanecki, Z., 2014, "Advances in the Development of a Microturbine Engine," ASME J. Eng. Gas Turbines Power, **136**(7), p. 071201.

[11] Casey, M. V., and Robinson, C., 2013, "A Method to Estimate the Performance Map of a Centrifugal Compressor Stage," ASME J. Turbomach., **135**(2), p. 21034.

[12] Casey, M. V., and Robinson, C., 2021, Radial Flow Turbocompressors, Cambridge University Press, New York.

[13] Aungier, R. H., 2000, Centrifugal Compressors, ASME Press, New York.

[14] Rusch, D., and Casey, M. V., 2013, "The Design Space Boundaries for High Flow Capacity Centrifugal Compressors," ASME J. Turbomach., **135**(3), p. 031035.

[15] Came, P. M., and Robinson, C. J., 1998, "Centrifugal Compressor Design," Proc. Inst. Mech. Eng., **213**(2), pp. 139–155.

[16] Aungier, R. H., 1995, "Mean Streamline Aerodynamic Performance Analysis of Centrifugal Compressors," ASME J. Turbomach., **117**(3), pp. 360–366.

[17] Aungier, R. H., 1995, "Centrifugal Compressor Stage Preliminary Aerodynamic Design and Component Sizing," ASME Paper No. 95-GT-078.

[18] Sirakov, B., and Casey, M., 2013, "Evaluation of Heat Transfer Effects on Turbocharger Performance," ASME J. Turbomach., **135**(2), p. 021011.

[19] Stanitz, J. D., 1952, "One-Dimensional Compressible Flow in Vaneless Diffusers of Radial-and Mixed-Flow Centrifugal Compressors, Including Effects of Friction, Heat Transfer and Area Change," Lewis Flight Propulsion Laboratory, Cleveland, OH, Report No. NACA-TN-2610.

[20] Dubitsky, O., and Japikse, D., 2008, "Vaneless Diffuser Advanced Model," ASME J. Turbomach., **130**(1), p. 011020.

[21] Sakurai, T., Yuasa, S., Honda, T., and Shimotori, S., 2009, "Heat Loss Reduction and Hydrocarbon Combustion in Ultra-Micro Combustors for Ultra-Micro Gas Turbines," Proc. Combust. Inst., **32**(2), pp. 3067–3073.

[22] Sadasivuni, V., and Agrawal, A. K., 2009, "A Novel Meso-Scale Combustion System for Operation With Liquid Fuels," Proc. Combust. Inst., **32**(2), pp. 3155–3162.

[23] Yuasa, S., Oshimi, K., and Uehara, M., 2003, "Concepts and Combustion Characteristics of an Ultra-Micro and a Micro Combustor," International Gas Turbine Congress, Tokyo, Japan, Nov. 2–7, Paper No. IGTC2003Tokyo OS-108.

[24] Mohamad, A. A., 2005, "Combustion in Porous Media: Fundamentals and Applications," Transp. Phenom. Porous Media, **3**, pp. 287–304.

[25] Mujeebu, M. A., Abdullah, M. Z., Mohamad, A. A., and Bakar, M. A., 2010, "Trends in Modeling of Porous Media Combustion," Prog. Energy Combust. Sci., **36**(6), pp. 627–650.

[26] McBride, B. J., 2002, "NASA Glenn Coefficients for Calculating Thermodynamic Properties of Individual Species," John H. Glenn Research Center at Lewis Field, Cleveland, OH, Report No. NASA/TP-2002-211556.

[27] Isomura, K., Murayama, M., Teramoto, S., Hikichi, K., Endo, Y., Togo, S., and Tanaka, S., 2006, "Experimental Verification of the Feasibility of a 100 W Class Micro-Scale Gas Turbine at an Impeller Diameter of 10 mm," J. Micromech. Microeng., **16**(9), pp. S254–S261.

[28] Liu, J., Zhang, D., Hou, L., Yang, J., and Xu, G., 2022, "Laminar Burning Speed of Aviation Kerosene at Low Pressures," Energies, **15**(6), p. 2191.

[29] Giovannoni, V., Sharma, R. N., and Raine, R. R., 2017, "Thermal Performances of a Small-Scale Regenerative Combustion Chamber for Ultra-Micro Gas Turbine," Combust. Sci. Technol., **189**(11), pp. 1859–1877.

[30] Dietrich, B., Schabel, W., Kind, M., and Martin, H., 2009, "Pressure Drop Measurements of Ceramic Sponges—Determining the Hydraulic Diameter," Chem. Eng. Sci., **64**(16), pp. 3633–3640.

[31] Casey, M. V., and Fesich, T. M., 2010, "The Efficiency of Turbocharger Compressors With Diabatic Flows," ASME J. Eng. Gas Turbines Power, **132**(7), p. 72302.

[32] Rodgers, C., and Geiser, R., 1987, "Performance of a High-Efficiency Radial/Axial Turbine," ASME J. Turbomach., **109**(2), pp. 151–154.

[33] Whittfield, A., 1990, "The Preliminary Design of Radial Inflow Turbines," ASME J. Turbomach., **112**, pp. 50–57.

[34] Moustapha, H., Zelesky, M. F., Baines, N. C., and Japikse, D., 2003, *Axial and Radial Turbines*, Concepts NREC, White River Junction, VT.

[35] Ventura, C., Jacobs, P. A., Rowlands, A. S., Petrie-Repar, P., and Sauret, E., 2012, "Preliminary Design and Performance Estimation of Radial Inflow Turbines: An Automated Approach," ASME J. Fluids Eng., **134**(3), p. 031102.

[36] Demierre, J., Rubino, A., and Schiffmann, J., 2015, "Modeling and Experimental Investigation of an Oil-Free Microcompressor-Turbine Unit for an Organic Rankine Cycle Driven Heat Pump," ASME J. Eng. Gas Turbines Power, **137**(3), p. 032602.

[37] Mounier, V., Olmedo, L. E., and Schiffmann, J., 2018, "Small Scale Radial Inflow Turbine Performance and Pre-Design Maps for Organic Rankine Cycles," Energy, **143**, pp. 1072–1084.

[38] Aungier, R. H., 2006, *Turbine Aerodynamics*, ASME Press, New York.

[39] Badum, L., Prochaska, T., Schwentenwein, M., and Cukurel, B., 2024, "Ceramic and Metal Additive Manufacturing of Monolithic Rotors From Sialon and Inconel and Comparison of Aerodynamic Performance for 300 W Scale Microturbines," ASME J. Eng. Gas Turbines Power, **146**(2), p. 021006.

[40] Cho, S. K., Lee, J., and Lee, J., 2018, "Comparison of Loss Models for Performance Prediction of Radial Inflow Turbine," Int. J. Fluid Mach. Syst., **11**(1), pp. 97–109.

[41] Suhrmann, J. F., Peitsch, D., Gugau, M., Heuer, T., and Tomm, U., 2010, "Validation and Development of Loss Models for Small Size Radial Turbines," ASME Paper No. GT2010-22666.

[42] Chen, H., and Baines, N. C., 1994, "The Aerodynamic Loading of Radial and Mixed-Flow Turbines," Int. J. Mech. Sci., **36**(1), pp. 63–79.

[43] Futral, S. M., and Wasserbauer, C. A., 1965, "Off-Design Performance Prediction With Experimental Verification for a Radial-Inflow Turbine," NASA, Cleveland, OH, Report No. TN D-2621.

[44] Paltrinieri, A., 2014, "A Mean-Line Model to Predict the Design Performance of Radial Inflow Turbines in Organic Rankine Cycles," Master thesis, Department of Industrial Engineering, University of Padova, Padova, Italy.

[45] Jansen, W., 1967, "A Method for Calculating the Flow in a Centrifugal Impeller When Entropy Gradient Are Present," Royal Society Conference on Internal Aerodynamics, Cambridge, UK, July 19–21, pp. 133–146.

[46] Rodgers, C., 1967, "Efficiency and Performance Characteristics of Radial Turbines," SAE Trans., **75**, pp. 681–692.

[47] Bergman, T. L., Incropera, F. P., DeWitt, D. P., and Lavine, A. S., 2011, *Fundamentals of Heat and Mass Transfer*, Wiley, New York.

[48] Nachouane, A. B., Abdelli, A., Friedrich, G., and Vivier, S., 2015, "Numerical Approach for Thermal Analysis of Heat Transfer Into a Very Narrow Air Gap of a Totally Enclosed Permanent Magnet Integrated Starter Generator," IEEE Energy Conversion Congress and Exposition, Montreal, QC, Canada, Sept. 20–24, pp. 1749–1756.

[49] Tanaka, S., Esashi, M., Isomura, K., Hikichi, K., Endo, Y., and Togo, S., 2007, "Hydroinertia Gas Bearing System to Achieve 470 m/s Tip Speed of 10 mm-Diameter Impellers," ASME J. Tribol., **129**(3), pp. 655–659.

[50] Peirs, J., Waumans, T., Vleugels, P., Al-Bender, F., Stevens, T., Verstraete, T., Stevens, S., et al., 2007, "Micropower Generation With Microgasturbines: A Challenge," Proc. Inst. Mech. Eng., Part C, **221**(4), pp. 489–500.

[51] Seo, J., Lim, H. S., Park, J., Park, M. R., and Choi, B. S., 2017, "Development and Experimental Investigation of a 500-W Class Ultra-Micro Gas Turbine Power Generator," Energy, **124**, pp. 9–18.

[52] Dessornes, O., and Zwyssig, C., 2010, "Micro-Generator for Ultra Micro Gas Turbine," Power MEMS 2010, Leuven, Belgium.

[53] International Organization for Standardization, 2017, *ISO 15:2017: Rolling Bearings—Radial Bearings—Boundary Dimensions, General Plan*, International Organization for Standardization, Geneva, Switzerland.

[54] Zwyssig, C., and Kolar, J. W., 2006, "Design Considerations and Experimental Results of a 100 W, 500 000 Rpm Electrical Generator," J. Micromech. Microeng., **16**(9), pp. S297–S302.

[55] Zwyssig, C., 2008, "An Ultra-High-Speed Electrical Drive System," Ph.D. dissertation, Eidgenössische Technische Hochschule Zürich, Zurich, Switzerland.

[56] Pfister, P., and Perriard, Y., 2010, "Very-High-Speed Slotless Permanent-Magnet Motors: Analytical Modeling, Optimization, Design, and Torque Measurement Methods," IEEE Trans. Ind. Electron., **57**(1), pp. 296–303.

[57] Luomi, J., Zwyssig, C., Looser, A., and Kolar, J. W., 2009, "Efficiency Optimization of a 100-W 500 000-r/Min Permanent-Magnet Machine Including Air-Friction Losses," IEEE Trans. Ind. Appl., **45**(4), pp. 1368–1377.

[58] Hearn, E., 1997, *Mechanics of Materials 2: The Mechanics of Elastic and Plastic Deformation of Solids and Structural Materials*, Butterworth-Heinemann, Oxford, UK.

[59] Larsonneur, R., 1990, "Design and Control of Active Magnetic Bearing Systems for High Speed Rotation," Ph.D. dissertation, ETH Zurich, Zurich, Switzerland.

[60] Polinder, H., 1998, "On the Losses in a High-Speed Permanent-Magnet Generator With Rectifier," Ph.D. dissertation, University of Delft, Delft, NL.

[61] Borisavljevic, A., 2012, "Limits, Modeling and Design of High-Speed Permanent Magnet Machines," Ph.D. dissertation, University of Delft, Delft, NL.

[62] Liu, N., Hung, K., Yang, S., Lee, F., and Liu, C., 2020, "Design of High-Speed Permanent Magnet Motor Considering Rotor Radial Force and Motor Losses," Energies, **13**(22), p. 5872.

[63] Bilgen, E., and Boulos, R., 1973, "Functional Dependence of Torque Coefficient of Coaxial Cylinders on Gap Width and Reynolds Numbers," ASME J. Fluids Eng., **95**(1), pp. 122–126.

[64] Mack, M., 1967, "Luftreibungsverluste Bei Elektrischen Maschinen Kleiner Baugrösse," Dissertation, University of Stuttgart, Stuttgart, Germany.

[65] Burnand, G. P.-A., 2017, "Validation by Measurements of a Windage Losses Model for Very-High-Speed Machines," International Conference on Electrical Machines and Systems, Sydney, NSW, Australia, Aug. 11–14, Vol. 20, pp. 1–4.

[66] Burnand, G., Araujo, D. M., and Perriard, Y., 2018, "Optimization of Shape and Topology for Slotless Windings in BLDC Machines," International Conference on Electrical Machines and Systems, Jeju, Korea, Oct. 7–10, Vol. 21, pp. 31–36.

[67] Gibson, L., Galloway, L., Kim, S. I., and Spence, S., 2017, "Assessment of Turbulence Model Predictions for a Centrifugal Compressor Simulation," J. Global Power Propul. Soc., **1**, pp. 142–156.

[68] Verstraete, T., Alsalihi, Z., and van den Braembussche, R. A., 2010, "Multidisciplinary Optimization of a Radial Compressor for Microgas Turbine Applications," ASME J. Turbomach., **132**(3), p. 031004.

[69] Javed, A., Arpagaus, C., Bertsch, S., and Schiffmann, J., 2016, "Small-Scale Turbocompressors for Wide-Range Operation With Large Tip-Clearances for a Two-Stage Heat Pump Concept," Int. J. Refrig., **69**, pp. 285–302.

[70] Balat-Pichelin, M., and Bousquet, A., 2018, "Total Hemispherical Emissivity of Sintered SiC Up to 1850 K in High Vacuum and in Air at Different Pressures," J. Eur. Ceram. Soc., **38**(10), pp. 3447–3456.

[71] Paolini, C. P., and Bhattacharjee, S., 2012, "IGE Model: An Extension of the Ideal Gas Model to Include Chemical Composition as Part of the Equilibrium State," J. Thermodyn., **2012**, pp. 1–18.